ROTATIONAL SHEAR INTERFEROMETRY
FOR ASTRONOMICAL IMAGING

BY

BRISTOL JAMES CRAWFORD

B.S., Duke University, 2002

HONORS THESIS

Submitted in partial fulfillment of the requirements
for Graduation with Distinction in Physics
in the Trinity College of
Duke University, 2002

Durham, North Carolina

20030110 095

ROTATIONAL SHEAR INTERFEROMETRY
FOR ASTRONOMICAL IMAGING

Bristol James Crawford
Department of Physics
Trinity College
Duke University
Henry Everitt, Adviser

An astronomical imaging instrument was developed which coupled a rotational shear interferometer (RSI) to a telescope with numerical aperture (NA) matching optics. The instrument was designed and constructed. Computer software was written to assist in the NA matching and perform rudimentary wavelength filtering. The completed astronomical imaging instrument was used to image a synthetic binary star created out of light emitting diodes (LEDs) with varying separation and spectrum. Results show that the RSI/telescope combination can image sparse arrays of point sources with small angular separation. Atmospheric turbulence was introduced, and the RSI/telescope instrument was tested for sensitivity to phase distortions.

TABLE OF CONTENTS

LIST OF FIGURES

CHAPTER 1
INTRODUCTION AND BACKGROUND

1. Interferometry in Astronomy

1.1. Astronomical Imaging Limits

Traditionally, optical astronomy is conducted using a telescope with a lens. Light from a stellar object enters the telescope aperture, is focused by the mirror, and is then magnified using a secondary lens. The image of the object is then projected onto the eye or onto a camera. The angular resolution of a given telescope is theoretically limited by diffraction [1]. For a perfect telescope with diameter D, observing a wavelength λ, the highest possible angular resolution is given by [2]

$$\theta_R = \frac{2.52 \times 10^5 \lambda}{D} \qquad (1)$$

where θ_R is given in arc-seconds. Lowering the wavelength observed or increasing the diameter of the telescope will result in a better angular resolution. The Hubble Space Telescope (HST) is a Cassegrain type telescope with a 2.4 m diameter mirror. At a wavelength of λ=500 nm, the HST images with an angular resolution of ~0.05 arc-seconds.

However, for telescopes mounted on the ground, the experimental angular resolution does not approach the theoretical boundary. Light passing through the earth's atmosphere sees a constantly changing index of refraction due to turbulence. This leads to distortion of the wavefront as seen by the telescope. To calculate the effects of atmospheric turbulence on astronomical imaging, Fried introduced a simple model [2]. Light travels through earth's atmosphere instantaneously so we can ignore the depth of the atmosphere and assume that it is a shell with varying index across its surface. At any given moment in time, the shell can be broken into 10 cm square tiles over which the index is constant. Each of these tiles is called a stable cell [2]. For the time that light takes to travel through the atmosphere these cells remain constant since their index is changing on the order of a millisecond.

Fried's model states that planar starlight encountering the atmosphere is broken into 10 cm isoplanatic regions where the wavefront is still flat. However, over a larger area than 10 cm the plane wave from the star covers many stable cells and is randomly deformed due to path length differences of a few micrometers. This creates an undulating wavefront that changes unpredictably every millisecond [2]. For a telescope with an aperture of less than the stable cell size, 10 cm, starlight can be considered isoplanatic and the angular resolution of the telescope is limited by diffraction. But, for telescopes with an aperture spanning many stable cells, like the 10 m Keck telescopes, the planar starlight is randomly deformed over each cell. The image produced is the superposition of many diffraction limited 10 cm apertures. Therefore, the angular resolution of a 10 m telescope is the same as that of a 10 cm telescope, about 1 arc-second [2]. For telescopes located on earth without atmospheric correction the best

possible angular resolution is 1 arc-second, the diffraction limit of a 10 cm telescope. Larger telescopes will gather more light (light collection increases as d^2, where d is the diameter of the telescope), but they cannot image at a higher resolution. To image at the diffraction limit with a telescope on earth, astronomers need a method to correct for atmospheric distortions. Although there are ways to do this while still using conventional imaging methods (involving actuated mirrors, or placing the telescope above the atmosphere), interferometers offer a simpler method of correction.

1.2. Why Interferometry?

Interferometry has long been used in optical astronomy because it offers several benefits over conventional imaging methods. The benefits are primarily generated by the ability to do data processing of fringe patterns on a computer. Through data processing of astronomical fringe patterns it is possible to correct for atmospheric distortions, determine stellar diameters and binary star spacing [1], measure spatial and spectral information simultaneously, and see at the diffraction limit of ground-based telescopes. In some cases, like observation at radio wavelengths where traditional methods are not feasible, interferometry is used almost exclusively. Using an array of telescopes based in different countries, radio astronomers can create interferometers with long baselines. The effective aperture of the telescope array is given by the baseline, so these arrays can image objects much smaller than the diffraction limit of conventional optical imaging systems [1]. There are many types of interferometers used in astronomy, and each has different advantages and drawbacks.

1.3. Types of Interferometry used in Astronomy

1.3.1. Speckle Interferometry

Theoretically, speckle interferometers make it possible to counteract the effects of changing atmospheric distortion because the exposure time is instantaneous so the atmosphere can be considered static. Due to the random shifts of atmospheric turbulence, the photons counted by the CCD create a speckle pattern similar to laser light diffusion [1]. Each individual speckle is only limited in angular resolution by diffraction. For a source small in angular size, the photons travel nearly identical paths through the atmosphere and encounter the same distortions. The image of the source is built up by the individual speckles, and this makes it possible to image at the theoretical diffraction limit of a telescope [1]. Experimentally, the exposure time is on the order of a few milliseconds, so there is still some amount of distortion introduced, but this is negligible compared to the distortions introduced over a long exposure on a traditional imaging system, which can be up to several minutes. Astronomers have been able to image objects with visual magnitude 16 or 17 using speckle interferometry [1]. However, this method has a poor signal-to-noise ratio (SNR) for bright sources, when compared to other types of interferometry [1]. The advantage is that in speckle interferometry atmospheric distortion is constant over the exposure time, although it does not correct for the distortions. Astronomers turn to other types of interferometry for atmospheric corrections.

1.3.2. Radio Interferometry

When making the shift from observing at visual wavelengths to radio wavelengths, a much larger telescope is needed for conventional imaging methods. As can be seen from eq. 1, to resolve one arc-second an astronomer needs a 1 m telescope at visual wavelengths, and a 10 km telescope at radio wavelengths [1]. Clearly this is not

realistic. Out of necessity, radio astronomers have turned to interferometry to conduct observations, and these interferometers are in wide usage. Two types of interferometers are now used, the very-large-array (VLA), and the very-long-baseline interferometer (VLBI) [3]. The VLA consists of many telescopes working in unison, whereas the VLBI utilizes two telescopes with a large spacing between them (e.g. diameter of earth). Assuming a wavelength of 1 cm, and a baseline of 10,000 km, a radio interferometer has an angular resolution of 25 milliarc-seconds. Therefore, these interferometers are capable of resolving radio emitting objects 10^3 times smaller then the ground-based resolution limit of optical telescopes [1]. Radio astronomy is also relatively unaffected by atmospheric distortion. The principles of radio astronomy, in particular the use of a long-baseline, have been successfully adapted to optical wavelengths. Using baselines of up to 200 m, astronomers have obtained sub-milliarc-sec resolution, but this can only be applied to objects brighter than visual magnitude 2. These long-baseline optical interferometers are highly susceptible to vibration [1], and are affected by atmospheric distortions; so another benefit of radio astronomy is lost in the transition.

1.3.3. Michelson Type Interferometry

Sometimes called pupil-plane interferometry, Michelson type shearing interferometers measure the coherence between different points on the wavefront by splitting the incoming light and then shearing one beam with respect to the other. Each of the three types performs a different shear on the wavefront. These differences are illustrated in Figure 1.1. Michelson type interferometers have a better SNR for bright objects than speckle interferometers; however, the longer exposure time increases the effects of atmospheric distortion. In order to obtain both spatial and spectral information,
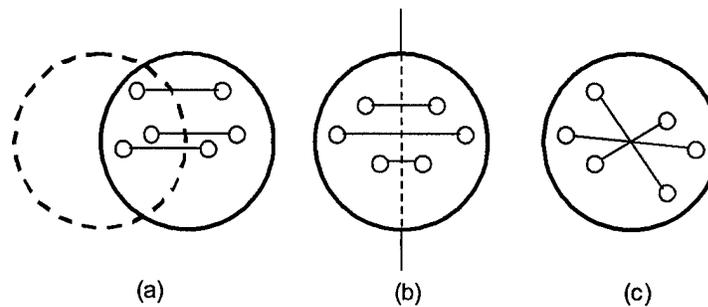
Figure 1.1: Examples of various types of shears used in shearing interferometry. (a) Lateral shear interferometer, (b) folding interferometer, (c) rotational shear interferometer (at 180° shear). Interfering points are connected with a straight line. Figure taken from Roddier [1].

a series of images must be taken while dithering the length of one of the interferometers arms. Each of these fringe images will have a different atmospheric distortion than the others, and this necessitates atmospheric correction. The major drawback of Michelson type interferometry is that, according to the Zernike theorem, it is limited to the observation of small objects [1]. However, it is well suited for the observation of binary star systems and other sparse arrays of point sources [4].

There are three basic variations of the Michelson interferometer that are used in optical astronomy. These interferometers measure the spatial degree of coherence of light by interfering different points on the wavefront without a phase shift due to optical path length difference. Through knowledge of the degree of coherence an image of the source can be recovered by the van Cittert-Zernike Theorem, to be discussed in Chapter 2 [5]. The first Michelson variation is the lateral shear interferometer, which measures the spatial coherence between points on the wavefront by shifting one beam with respect to the other [1]. Consequently, the beams only partially overlap, and the fringes are generated by only a fraction of the captured light. As the spacing between the interfering points increases, the efficiency of the interferometer drops. This loss of photons, coupled

with the fact that Michelson interferometers inherently reflect half of the input light, makes lateral shearing inefficient and not suitable for looking at dim objects.

Another type is the folding interferometer. In this variation, one of the flat mirrors of a Michelson interferometer is replaced with a right angle mirror. This measures the coherence of points reflected across the axis of the folding mirror. The two separated beams entirely overlap in this case, so no additional photons are lost after the inherent halving of the light. However, the interfering points on the wavefront are fixed, so this is not the most robust solution.

A third type of interferometer, similar to the folding interferometer, is the rotationally shearing interferometer (RSI). The RSI is a Michelson interferometer with two right angle mirrors in place of the flat mirrors. One of these right angle mirrors is rotated with respect to the other. This allows the user to control which points of the wavefront are being interfered, and permits improvement of the SNR [1]. The two interfering light beams totally overlap so no additional photons are lost. The time needed to capture the fringe images is longer than the characteristic time scale for atmospheric distortion, but such distortions can be corrected during the data reduction process as shown by Itoh and Ohtsuka [6], and C. and F. Roddier [1].

2. RSI Astronomy

2.1. Benefits of RSI Astronomy

As outlined above, interferometers offer some specific benefits over conventional imaging systems when used in conjunction with a telescope. The RSI in particular lends itself well to several of these improvements. RSI research has been conducted in the past

with the major goals of correcting for atmospheric distortions and imaging extra-solar planets. Pupil-plane interferometry gives a measure of the spatial coherence between different points on the wavefront, and this yields an image of the source. While all three types of pupil-plane interferometry have the same basic characteristics, the RSI is a more robust interferometer than both the folding and the lateral shearing interferometer. The lateral shearing interferometer loses photons due to the partial overlap of the interfering light beams, and the folding interferometer only interferes fixed points on the wavefront. The RSI joins the advantages of these two interferometers, giving total usage of the light and variation in interference points. Through data reduction techniques, a computer can analyze the fringes generated by the RSI and either correct for atmospheric distortion, or suppress a fringe pattern, thereby removing a star from the frame. In particular, this latter technique could lead to direct detection of extra-solar planets through the removal of the parent star from the image [7].

2.2. Research done

2.2.1. Experimental

M. Murty created the first wavefront folding interferometer in 1964 [8], and used it to measure the quality of right-angle prisms [9]. This was done using a modified Michelson interferometer with a plane mirror in one arm and a right-angle mirror in the other. The right angle mirror reversed the incoming rays so the wavefronts that recombined at the beam splitter formed mirror images of each other. When the right-angle mirror is exact, the fringes generated are predicted to be straight. By observing the deviation angle of the fringes, Murty was able to calculate the error in the right angle mirror [9].

Since then, experimental work involving the RSI has included both astronomical and non-astronomical applications. On the astronomical side, in 1985, C. and F. Roddier demonstrated RSI image reconstruction of both laboratory objects and the astronomical object Alpha Orionis [1,10]. The image obtained of Alpha Orionis was of sufficient quality to draw conclusions about the nature of the dust cloud surrounding the star and estimate Alpha Orionis' diameter [10].

More recently, Gallicchio demonstrated the ability of the RSI to image sparse arrays of point sources in the laboratory, recovering both spatial and spectral information [4]. Gallicchio used a beam splitter to project a HeNe laser and an Argon laser onto the same spot on a rotating diffuser. Using a portable RSI of his own design, Gallicchio then imaged this spot and obtained two points (due to the differing wavelengths of the sources) on the Fourier transform plane along the same line, but at different distances from the center of the image. He predicted this result through theory and showed the degeneracy between angular position and wavelength. Theoretically, this degeneracy can be broken by rotating the RSI with respect to the array of sources and taking another image [4]. Breaking the degeneracy yields a spatial image and spectrum of the point source array.

Outside of astronomy, the research group of D. Brady has attached an RSI instrument to a microscope to obtain high numerical aperture and high depth of field simultaneously [11]. After matching the numerical aperture of the RSI to that of the microscope using an array of lenses, Brady's group used the RSI to image diffraction masks placed in front of the microscope at different distances. The diffraction masks were illuminated by an incoherent light source, and the fringes generated by the RSI were

projected onto a CCD after passing through a spectral filter. Brady's group then demonstrated the ability of the RSI microscope to image two diffraction masks placed at different distances from the microscope objective simultaneously without any loss of numerical aperture [11].

D. Brady has also shown that the RSI can be used for tomographic 3D imaging using a quasi-monochromatic incoherent light source [5]. Brady reconstructed an opaque 3D object by rotating the object through 128 angles in front of the RSI aperture. At each of the 128 rotation points, the RSI recorded 8 frames of data on a 128×128 pixel array. Each of the 8 frames taken was at a different optical path delay, equally spaced over one wavelength. Using the cone-beam algorithm, the $128 \times 128 \times 128$ data cube was reconstructed into a 3D image of the object. This experiment demonstrates the transition of cone-beam tomography from the x-ray region of the spectrum to visible light [5].

K. Itoh has used the RSI to demonstrate supermultispectral and spatial imaging simultaneously [12]. Itoh successfully imaged a variety of sources, both self-radiating and externally illuminated with incoherent light. Each of the images was the result of the 3D Fourier transform of a series of 64 or 128 fringe patterns, each of size 64×64 pixels, taken at differing optical path delays. The output of each image included a spatial map of the object and an entirely separate spectrum [12].

2.2.2. Theoretical

The majority of the astronomy-related research involving the RSI has been done theoretically. The theory can be broken down into two main areas: the consideration of atmospheric corrections, and the detection of extra-solar planets. K. Itoh asserts that for the RSI to be used on earthbound large telescopes, an algorithm must be developed to

correct for atmospherically disturbed interferograms [8]. He suggests a method similar to speckle interferometry. To create RSI images containing both spatial and spectral information, one of the arms of the interferometer must be dithered to change the optical path difference. At each of the optical path delays, an image is captured leading to the creation of a data cube. Itoh suggests that if each individual frame is captured in 10 ms or less the atmospheric disturbance can be neglected, just like in speckle interferometry. However, since many of these frames are needed to generate spectral information, the atmospheric distortion cannot be neglected over the time required to generate the entire image. The solution to this problem is to do repeated rapid scanning, generating multiple images of the same object. Then through additional data processing, Itoh predicts that a corrected image without atmospheric distortion can be generated [8].

Another technique for restoring atmospherically disturbed images, non-specific to the RSI, is proposed by W.T. Rhodes and J.W. Goodman [13]. Rhodes and Goodman consider the aperture of the imaging system to be broken into infinitely many pinholes in an aperture mask. Each individual pinhole contributes an interference term to the fringe pattern for each possible pairing. When the wavefront entering the aperture is distorted, the phase is changed between each pair of points. Then each pair of points on the mask with equal spacing adds with a different phase from the other pairs, leading to a loss of contrast. Rhodes and Goodman consider the loss of fringe contrast a factor of this pinhole pair redundancy. They devise a method using an aperture mask with finite pinholes to remove the redundancy, and then through data reduction, the distortion of the wavefront can be corrected [13]. However, the use of a mask over the aperture of the

imaging system blocks incoming light, and this may not be an optimal method for imaging dim objects.

R. Dou introduced a new class of algorithms for high-resolution phase distortion suppression and then simulated the efficiency of the method [14]. Using either a Mach-Zehnder interferometer or an RSI, Dou obtained a fringe pattern from a distorted wavefront. He then fed the information gathered from the fringe pattern through a computer, and into a feedback loop with the interferometer imaging system. By placing a spatial light modulator between the distortion and the RSI and connecting it to the computer, Dou altered the phase of the distorted wave point-by-point depending on the distortion information obtained by the computer. Making use of the iterative algorithm he developed, this feedback successfully suppressed wavefront distortions [14].

R.P. Korechoff and M.S. Scholl have independently simulated extra-solar planet detection on the RSI using a nearly identical method [7,15]. The method assumes that a planet/star system is composed of two point sources, of which one is many times brighter than the other. Since there is some spacing between the planet and the star, the plane waves reaching earth from the two point sources have slightly different directions of propagation. Thus, by pointing an RSI directly at the star, the plane wave propagating from the star moves along the optical axis of the RSI, whereas the wave from the planet is slightly tilted with respect to the axis. When the RSI is kept at null the star's wavefront destructively interferes with itself at every point. This, in theory, removes the star from the fringe pattern, leaving only the fringes generated by the nearby planet. Experimentally, this method will be limited because the star has finite size and cannot be directly on the optical axis. However, Korechoff theorizes that three orders of magnitude

of starlight suppression can be expected even with experimental inaccuracies introduced. His ideal experimental setup includes a Cassegrain type telescope complete with adaptive optics to correct for atmospheric distortions [7]. Using this method, an RSI has the capability of interferometrically imaging an extra-solar planet [7,15].

These theoretical papers give a firm basis for the development of an RSI astronomical instrument to correct for atmospheric distortions and observe extra-solar planets. However, many of the experiments proposed and supported by this research have not yet been conducted.

3. Goals of Research

This project focuses on demonstrating RSI imaging for astronomy. There have been few astronomical RSI imaging experiments, and there has not been any new experiment done since the mid 1980's. Recent theory surrounding the RSI has not been demonstrated in the lab. To that end, this project focuses on coupling an RSI to a 10" Newtonian telescope by matching their respective numerical aperture. Then a synthetic binary star will be imaged. Once the proof of concept phase of the project is completed, the newly fabricated RSI instrument will be coupled to the 32" telescope at Three College Observatory (TCO). The project will then focus on directly imaging a binary that is unresolvable using traditional imaging methods on large earth-based telescopes. This will involve the atmospheric distortion corrections that are described in the literature. These corrections will be done using computational Fourier analysis on the fringes generated by the RSI. Upon completion, we will have created a dedicated, functioning

RSI instrument for use in astronomy, complete with simultaneous spatial/spectral imaging and computer-based atmospheric correction.

CHAPTER 2
ROTATIONAL SHEAR INTERFEROMETER
THEORY

1. Introduction

The Rotational Shear Interferometer (RSI) is a type of wavefront folding interferometer that is very similar in construction to the Michelson interferometer. The RSI generates fringe patterns that contain both spatial and spectral information because it measures the temporal and spatial coherence of light simultaneously. This ability has led to the adoption of the RSI for many uses, including astronomical imaging, 3D visible light tomography [5], and microscopy [11].

This project aims to develop the RSI into a functional astronomical imaging instrument, and thus does not make use of the high depth of field provided by the RSI and discussed by Brady and Potuluri [5,11]. Astronomical imaging takes place in the far field, so the following theoretical discussion will not consider the 3D imaging capabilities of the RSI, and will focus primarily on point sources. Since the RSI is similar to the Michelson interferometer, the discussion will begin by analyzing the Michelson for its spectral imaging abilities. Then it will consider how the RSI creates spatial images of
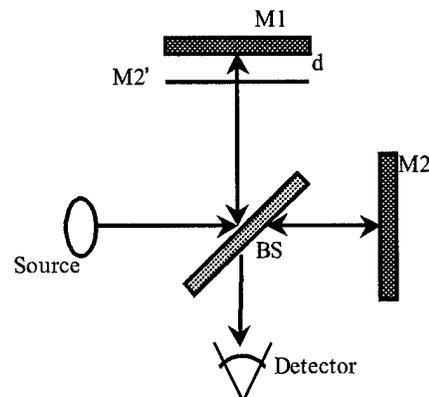
Figure 2.1: Michelson Interferometer. Light enters from the source on the left, gets separated by the beam splitter and travels towards the two mirrors, M1 and M2. The beams are recombined at the beam splitter and projected onto the detector. Mirror M1 is placed a distance d farther from the beam splitter than mirror M2. Therefore, light reflected from M1 travels a distance 2d farther than light from M2. The path length difference creates the retardation time $\tau = \dfrac{2d}{c}$.

point sources without measuring spectral information. The combination of these two theories creates a comprehensive discussion of the RSI for use in astronomical imaging.

2. The Michelson Interferometer

2.1. Construction and Operation

The Michelson interferometer is constructed out of two flat mirrors, a dithering stage, a beam splitter, and a detector, as seen in Figure 2.1. Light enters the interferometer and is divided by the beam splitter. The two beams travel down the arms of the interferometer and are reflected by the flat mirrors. These beams are then recombined in the beam splitter and projected onto the detector. One of the flat mirrors is kept at a constant distance from the beam splitter, while the other mirror is placed on the dithering stage and allowed to move along the optical path. This creates an optical path difference between the two arms of the interferometer. When the beams are recombined

in the beam splitter there is a phase shift between the two, and they generate a fringe pattern due to constructive and destructive interference. This fringe pattern is captured using a detector, typically a CCD camera, and fed into a computer for analysis.

To analyze the spectrum of a source the Michelson takes a series of fringe pattern images. Each fringe pattern occurs at a different optical path delay controlled by the dithering stage. Combining the captured fringe patterns and knowledge of the optical path length difference at each point, the computer performs Fourier analysis to calculate the spectrum of the source. Intuitively, the computer knows the path length difference for each fringe pattern, and it can calculate the movement of the fringes from one optical path delay to the next. From this it can calculate the frequency of the light creating each fringe pattern, and recover the spectrum of the source. Now we turn to a theoretical explanation of the Michelson interferometer.

2.2. Michelson Theory

For the moment, consider a Michelson interfering monochromatic laser light. Then the interference pattern generated on the detector screen along the optical axis of the interferometer is given by [16]

$$I = I_1 + I_2 + \sqrt{I_1 I_2} \cos\left(\frac{2\omega d}{c}\right) \tag{1}$$

where ω is the frequency of the light, I_1 and I_2 are the intensities of the two interfering beams, and d is the path length difference between the two arms of the interferometer. It is clear that this interference pattern varies as a cosine wave, and that as d increases there will be no change in the variation of the field. The Michelson interferometer makes it possible to interfere wavefronts generated at different times from the same source. The relation between the two wavefronts is called coherence. Since the interfering

wavefronts are separated only by time, this is called temporal coherence [16]. Laser light is a temporally coherent source so the wavefront generated at one time is identical to the wavefront generated at any other time. That is why the interference varies as a cosine function regardless of the value of d. This is not generally the case. For partially coherent light, as d continues to increase and the wavefronts are separated by more time, the interference term will drop to zero and there will be no fringes. The consideration of partially coherent and incoherent light requires a more rigorous explanation of interference.

Consider a source that emits waves of the form

$$E(t) = A(t)\exp\{i[\omega_0 t + \phi(t)]\}$$

The mutual coherence function is defined by a correlation between two waves of form $E(t)$[2]

$$\Gamma_{12}(\tau) = \langle E_1(t)E_2^*(t-\tau)\rangle \tag{2}$$

This is a relation between the two waves generated at a source, separated by a retardation time τ. $\Gamma_{12}(\tau)$ is normalized to get the complex degree of coherence [2]

$$\gamma_{12}(\tau) = \frac{\langle E_1(t)E_2^*(t-\tau)\rangle}{\sqrt{\langle |E_1(t)|^2\rangle\langle |E_2(t)|^2\rangle}} \tag{3}$$

The interference generated by the Michelson interferometer can then be rewritten using the complex degree of coherence, and we find that [2]

$$I = I_1 + I_2 + \sqrt{I_1 I_2}\, \mathrm{Re}\,\gamma_{12}(\tau) \tag{4}$$

This formula for I is called the "general interference law for partially coherent light [2]." The complex degree of coherence is used both for temporal coherence and for spatial

coherence. Temporal coherence measures the similarity between two wavefronts separated by time. It is a measure of the wave's properties along the direction of propagation, and is related directly to the spectrum of the source [16]. A perfect monochromatic source is temporally coherent. Spatial coherence measures the similarity between two points on one wavefront. It is a measure of the wave's properties transverse to the direction of propagation [16]. A perfect plane wave is spatially coherent. In the current discussion, τ is the retardation time introduced by the arms of the Michelson interferometer. Later, spatial coherence will be considered and the meaning of τ will change.

Now return to the earlier discussion of laser light. Assuming that the beam splitter is 50/50, then $I_1 = I_2 = I_0$. The retardation time for the Michelson interferometer is $\tau = \dfrac{2d}{c}$. Eq. 1 can be rewritten into [16]

$$I = 2I_0[1 + \cos(\omega\tau)] \tag{5}$$

For this case, the complex degree of coherence is $\gamma(\tau) = \cos(\omega\tau)$, and the light is temporally coherent. It is clear that the Fourier transform of eq. 5 will recover the spectral information for the laser, and the spectrum will consist of one frequency, ω.

The Michelson interferometer measures temporal coherence, and through Fourier analysis, recovers the spectrum of a source. While this discussion has only used the example of monochromatic light, eq. 4 makes it possible to calculate the fringe pattern generated by any source, monochromatic or otherwise. The RSI makes use of the spectral analysis provided by the Michelson, and measures spatial information
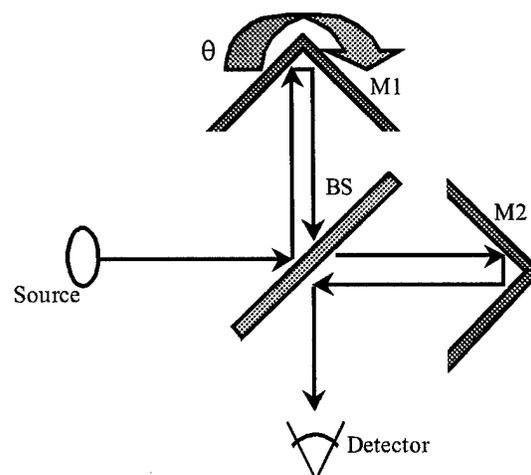
Figure 2.2: Rotational Shear Interferometer. A modified version of the Michelson interferometer. The path length between the beam splitter and the right angle mirrors M1 and M2 is kept constant. To measure the spatial coherence of a source, mirror M1 is rotated an angle θ about the optical axis. This rotates one wavefront an angle 2θ with respect to the other. The beams are recombined at the beam splitter, and the fringes are projected onto the detector.

simultaneously. The complex degree of coherence introduced above will prove important

when discussing spatial coherence in the next section.

3. The Rotational Shear Interferometer (RSI)

3.1. Construction and Operation

The RSI is obtained from a Michelson interferometer by removing the two flat

mirrors of the Michelson and replacing them with right angle mirrors as seen in Figure

2.2. The right angle mirrors preserve the handedness of the light and make it possible to

rotate one wavefront with respect to the other. One of the right angle mirrors is rotated

an angle θ about the optical axis of the interferometer. This has the effect of rotating one

wavefront an angle of 2θ about the optical axis. If the optical path length between the

two arms is kept equal, then the RSI measures the spatial coherence of the light and not

the temporal coherence. The measurement of the spatial coherence can be used to

recover an image of the source, as predicted by the van Cittert-Zernike Theorem [2]. If the optical path difference is varied the spectrum of the source can be measured, just like in the Michelson interferometer.

Most of the time the RSI is in use, a narrow-band filter (Figure 3.4) forces the light to be quasi-monochromatic. In this case the RSI is not used to determine the spectral information since that would be unnecessary. To obtain the spatial information from the source, the shear angle θ is set where there is good fringe visibility. Then, even though there is no spectral analysis, one of the optical path lengths is varied by the dithering stage. Each of the fringe patterns is captured by the CCD camera and sent to the computer. The computer uses the multiple fringe patterns to filter for the fringes generated by the known wavelength of the spectral filter, as discussed in Chapter 3. This helps to eliminate background noise. After filtering, the computer performs a Fourier transform to obtain the spatial information. It has been shown that the RSI can measure both spatial and spectral information simultaneously [12].

3.2. RSI Theory

To understand the physics of the RSI, first look at Young's two-slit experiment, shown in Figure 2.3. Now make use of the complex degree of coherence described by eq. 3. In the previous example, we considered an interferometer that measured temporal coherence. The two-slit experiment measures the spatial coherence between two points on the wavefront, but since this is accomplished by redefining the retardation time τ, the same equations are used [16]. As before, the complex degree of coherence is defined by

$$\gamma_{12}(\tau) = \frac{\langle \mathbf{E}_1(t)\mathbf{E}_2^*(t-\tau)\rangle}{\sqrt{\langle |\mathbf{E}_1(t)|^2\rangle\langle |\mathbf{E}_2(t)|^2\rangle}} \tag{6}$$
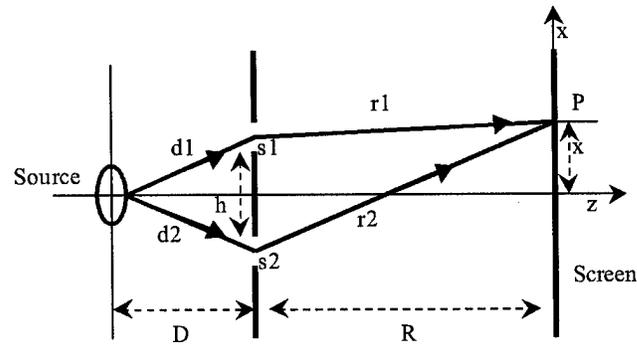
Figure 2.3: Young's Two-Slit Experiment. Light from a source passes through two slits, s1 and s2, separated by a distance h. The light then produces an interference pattern on the screen. This experiment measures spatial coherence by comparing two points on the wavefront.

where the electric field is now a vector quantity. The retardation time is found from

Figure 2.3. Light traveling through s1 to point P takes $t_1 = \dfrac{d_1 + r_1}{c}$ to reach the screen.

Light traveling through s2 takes $t_2 = \dfrac{d_2 + r_2}{c}$. Assuming the source is a point, and is

halfway between s1 and s2, then $d_1 = d_2$, and the retardation time is

$$\tau = \frac{r_2 - r_1}{c} \tag{7}$$

Then the fringes at a point on the detector plane are given by eq. 4. Although the two-slit experiment measures the spatial coherence of light, there is a temporal coherence measurement as well due to the path length difference seen in Figure 2.3. This path length difference is negligible since $r_1, r_2 \ll c$ and $\tau \approx 0$. For the simplest mode of operation of the RSI, the optical path lengths are kept equal between the two arms of the interferometer. It is then possible to measure the spatial coherence of the light without introducing a temporal phase shift. The path length difference in Young's two-slit experiment is vanishingly small, and therefore can be neglected. This makes it possible

to consider the RSI an extension of the 1D two-slit experiment to two dimensions. For the following description of the RSI the retardation time is ignored and the mutual intensity between two points on the wavefront is calculated directly.

As mentioned above, the simplest form of the RSI does not create an optical path length difference between the two arms. Now consider a point source placed far away from the RSI and slightly off the optical axis, and calculate the fringe pattern produced on the detector directly. Let ϕ_x, ϕ_y be the angular displacement of the source from the optical axis of the RSI, and let (x_c, y_c) be a point on the CCD camera. Following the light through the RSI we find that the interference is given by [4]

$$ I \propto 2 + 2\cos\left(\frac{4\pi\sin(2\theta)}{\lambda}\left(\tan(\phi_x)y_c + \tan(\phi_y)x_c\right)\right) \qquad (8) $$

It is important to note that in this formulation for the interference the wavelength λ, and the angular displacement of the source ϕ_x, ϕ_y both have contributions. This creates degeneracy between angular position and wavelength. As noted by Gallicchio, moving the object twice as far away, thus halving $\tan(\phi_x)$ and $\tan(\phi_y)$, and doubling the wavelength have the same effect on the interference pattern [4]. It is possible to break the degeneracy by rotating the RSI some amount $\Delta\phi_x$ about the optical axis, and taking a second image of the fringe pattern [4].

The RSI measures the mutual intensity function for two points on the wavefront [5,11]. The mutual intensity function for a point source placed far from the RSI and slightly off the optical axis has just been calculated. This mutual intensity function is a simplification of the complex degree of coherence since the RSI does not introduce an optical path delay. The mutual intensity function can be considered a form of the degree

of coherence. To obtain an image of the source from the fringes that form the mutual intensity function the van Cittert-Zernike Theorem is employed. This theorem states, "the complex degree of coherence is equal to the diffraction pattern of an aperture of the same size and shape as the source and illuminated by a spherical wave whose amplitude distribution is proportional to the intensity distribution across the source [16]." This is a relationship between the complex degree of coherence and the irradiance distribution across the extended source [2]. Through knowledge of the complex degree of coherence, and in this case, the mutual intensity function, an image of the source can be created using Fourier analysis. In the discussion of the two-slit experiment, it should be pointed out that the source image generated is only 1D. This is because the slits interfere two points on the wave front along one dimension. The RSI interferes points on the wavefront over the whole detector plane, and thus the Fourier transform of the fringes yields a 2D image of the source. This way, making use of the van Cittert-Zernike Theorem, images of sparse arrays of point sources can be generated using the mutual intensity function found for the RSI.

4. Spectral and Spatial Information

Although this discussion has focused on the spatial and spectral information gathering components separately, the RSI combines both of these abilities. The final goal of this project is to create an astronomical instrument from the RSI that can do both simultaneously. The introduction of right-angle mirrors into the Michelson interferometer led to the development of the RSI, but this did not change the spectral measurement capabilities of the interferometer. The RSI measures spatial coherence
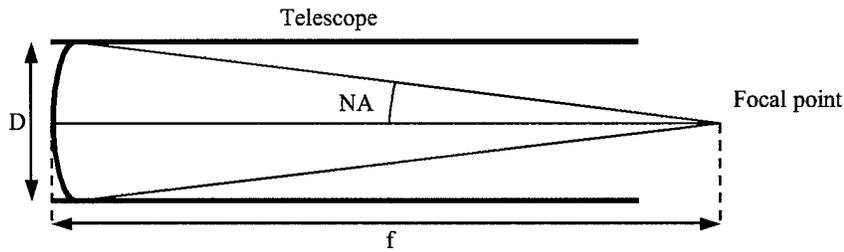
Figure 2.4: The numerical aperture (NA) of the telescope. The diameter of the mirror is D, the focal length of the mirror is f and the NA is defined as in eq. 9.

without changing the optical path length of the interferometer arms. Therefore, the RSI can measure the spatial coherence using one fringe pattern, and then dither one arm to measure the temporal coherence. Through Fourier analysis, the RSI can recover the spatial and spectral information from a source.

5. Geometrical Optics and Numerical Aperture Matching

5.1. Numerical Aperture Matching Constraints

In the experimental setup, light is collected by the telescope, passes through two lenses, and then enters the RSI that generates the fringe patterns recorded by the CCD. Both the telescope and the RSI have a numerical aperture (NA). The numerical aperture for the telescope is given by the equation

$$NA = 0.5\tan^{-1}\left(\frac{D}{f}\right) \tag{9}$$

In this equation, D is the diameter of the mirror and f is the focal length of the mirror. The physical meaning of the NA for a telescope can be seen in Figure 2.4. The numerical aperture for the RSI is given by the equation

$$NA = \frac{\lambda}{\Delta\sin\theta} \tag{10}$$

where λ is the wavelength of the light, Δ is the pixel size on the CCD, and θ is the shear angle of the RSI [11]. To minimize photon loss for the RSI/telescope combination imaging system, the NA of the telescope needs to be matched to the NA for the RSI. The two lenses between the telescope and the RSI are used for this purpose. These lenses must be placed precisely so that the light exiting the telescope couples into the RSI correctly. There are other constraints on the system for the coupling besides the matching of the NA. First, the spot size at the CCD cannot be larger than the CCD screen or photons will be lost. Also the total length of the optical system cannot be large due to the small size requirement on the final instrument. Then there are the physical restrictions of the optics, such as the focal lengths of the mirror and the two lenses and the initial source position.

These constraints form a set of parameters for calculating the lens placement for the matching optics. The input values for the system are the initial position of the source, the focal length of the mirror and of the two lenses, the diameter of the mirror and of the two lenses, the wavelength of the light, the shear angle of the RSI, the pixel size on the CCD, the total length restriction on the optical system, and the array size of the CCD. Given these values, the lens placement distances for the matching optics must be calculated. The computation is performed in <u>Mathematica</u> using geometrical optics and ray tracing.

5.2. Geometrical Optics and Ray Tracing

The <u>Mathematica</u> code used for the NA matching calculation is titled *abcd numerical aperture*, and can be found in Appendix A. The code traces a ray through the optical system as seen in Figure 2.5. This is done using geometrical optics. In
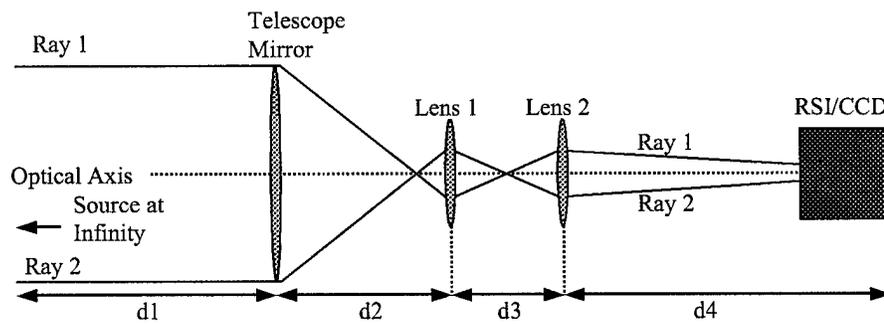
Figure 2.5: Tracing a ray through the optical system. The source is placed at infinity, so light entering the telescope mirror is collimated. The calculation considers the rays collected at the very top and bottom of the telescope mirror. When the NA of the telescope is matched to the NA of the RSI, the rays enter the RSI with the correct angle, and the spot size on the CCD is smaller than the CCD array.

geometrical optics the initial position of the ray is given as a vector of the form $\begin{pmatrix} x_0 \\ \gamma_0 \end{pmatrix}$,

where x_0 is the initial distance from the optical axis, and γ_0 is the initial trajectory of the ray with respect to the optical axis. For each optical element there is a transformation matrix. The two types of transformation for this experiment are translation through empty space and refraction through a lens. The corresponding transformation matrices can be found in Figure 2.6. Each optical element is assigned one of these matrices. The final position of the ray is then calculated by multiplying all the matrices and vectors together. This traces the ray through the optical system.
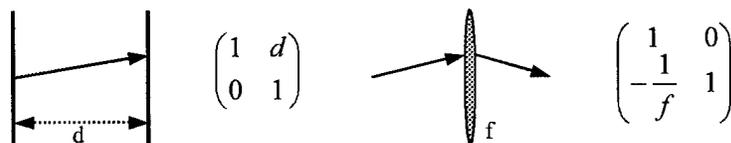
Figure 2.6: Transformation matrices for empty space and lens refraction. Figure taken from Guenther [16].

For the <u>Mathematica</u> calculation, instead of finding the final position and orientation of the ray, these values are given as a restriction. The code uses a system of three equations to solve for the lens placement distances (d2, d3, and d4 in Figure 2.5). In the experimental setup, the lenses are then placed at these distances and the NA aperture of

the telescope is matched to the RSI. The calculation can be viewed in Appendix A. Lens placement must be recalculated for every shear angle change on the RSI since the shear angle is used to calculate the NA of the RSI.

6. Fourier and Image Planes of the Source

A further complication on the NA matching process is the consideration of Fourier and image planes of the source. When light passes through a lens, the lens performs a Fourier transform on the light [16]. Consider collimated light entering a lens. The lens performs a Fourier transform on the light, and the lens becomes a Fourier plane of the source. Since the light is initially collimated, it is focused at the focal point of the lens. The focal point of the lens is the image plane of the source. If the source of the collimated light is a point source at infinity, then at the image plane there will be a single point of light. The image plane and the Fourier plane form a Fourier transform pair.

Now extend this to the RSI/telescope combination. First, the telescope mirror collects light from the source. Thus the telescope mirror is the Fourier plane of the source. This plane is easily identifiable due to the doughnut shape it takes, which will be discussed in Chapter 3. The telescope focuses the light from the source, and that is the image plane of the source. As the light collected by the telescope passes through the matching optics it passes through several different Fourier and image planes on its way to the RSI. Now, the RSI generates a fringe pattern of the light, and this is captured by the CCD. An image of the source is recovered by taking the Fourier transform of the fringe pattern. However, care must be taken that the fringe pattern is generated by the Fourier plane of the source. If the optics are misaligned and the image plane of the source

generates the fringe pattern on the CCD (i.e. the image plane of the source is at the CCD), then the Fourier transform of the fringe pattern will recover an image of the doughnut pattern that is the Fourier plane of the source. This happens because the Fourier plane and the image plane are a Fourier transform pair. Therefore, the fringe pattern must be generated by the doughnut pattern, and the Fourier plane must occur at the CCD screen for the Fourier transform to recover an image of the source. This is the final constraint on the NA matching calculation. For the imaging system to work properly, the doughnut pattern of the telescope mirror must appear on the CCD screen. When this occurs, the Fourier transform of the fringes will be an image of the source.

CHAPTER 3
EXPERIMENTAL DESIGN AND PROCEDURE

1. Overview of Laboratory

The goal of this project is to attach the portable rotational shear interferometer (RSI) designed by Gallicchio [4] to a telescope in the lab, and image a synthetic binary star. The major components used to do this are a telescope, a light source or other object to image, a portable RSI, a set of matching optics, a CCD, a computer, and a filter. The experimental setup can be seen in Figure 3.1. The telescope and the RSI are mounted on an optical bench and coupled through the set of matching optics. The matching optics consist of a flat mirror and two lenses designed to match the numerical aperture of the telescope to that of the RSI. The source is placed down a hallway directly in front of the telescope aperture. Light from the source is collected by the telescope and passed through the matching optics into the RSI. The RSI generates a fringe pattern that is filtered before being captured by the CCD camera. The captured fringe pattern is analyzed by the computer. The following is a more detailed description of the experimental setup.
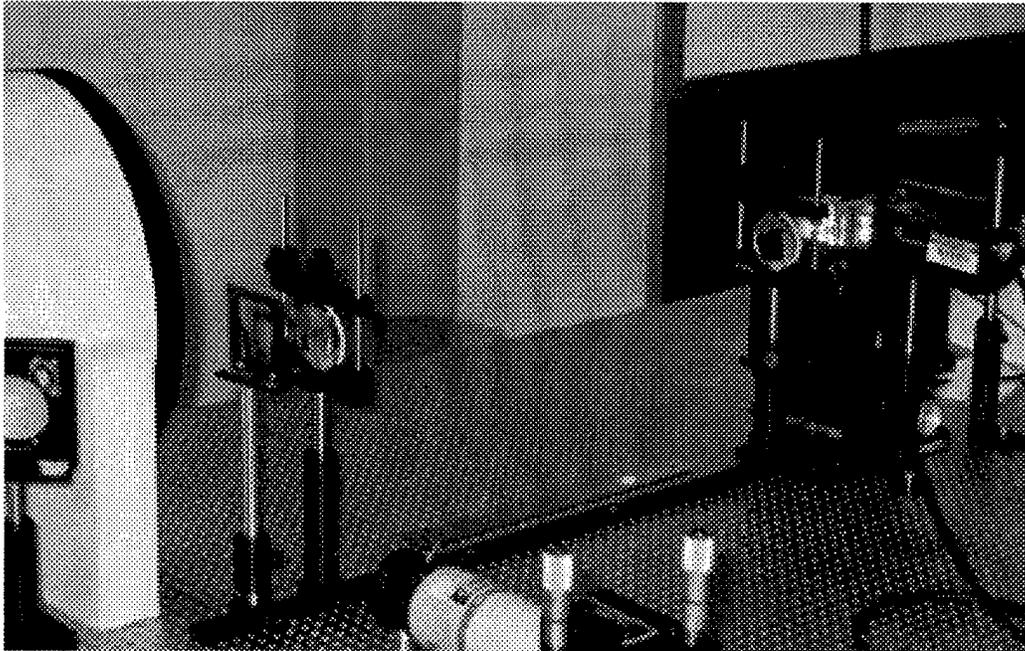
Figure 3.1: The experimental setup on the optical bench. The telescope and the flat mirror are on the left. The matching optics are on the rail in the center. The RSI and CCD camera are on the right.

2. Experimental Setup

2.1. Telescope and Matching Optics

The telescope that used is a Meade 10" Newtonian, with a focal length of 45" and an f-number of 4.5. The mirror is held inside a 42" tube with a diameter of 12 inches. A flat secondary mirror rests 37" from the mirror down the barrel of the tube, and reflects the light collected by the mirror off at a 90° angle. The secondary mirror blocks the center portion of the light collected by the telescope. Thus, the light exiting the side of the telescope looks like a disc with the center cut out. This pattern is called the doughnut pattern, and is important for finding the Fourier plane of the source as discussed in Chapter 2. Normally an eyepiece is placed on the barrel of the telescope, but this has been removed so the light passes out of the telescope without any additional magnification. The telescope is placed on one end of an optical bench so that the mirror
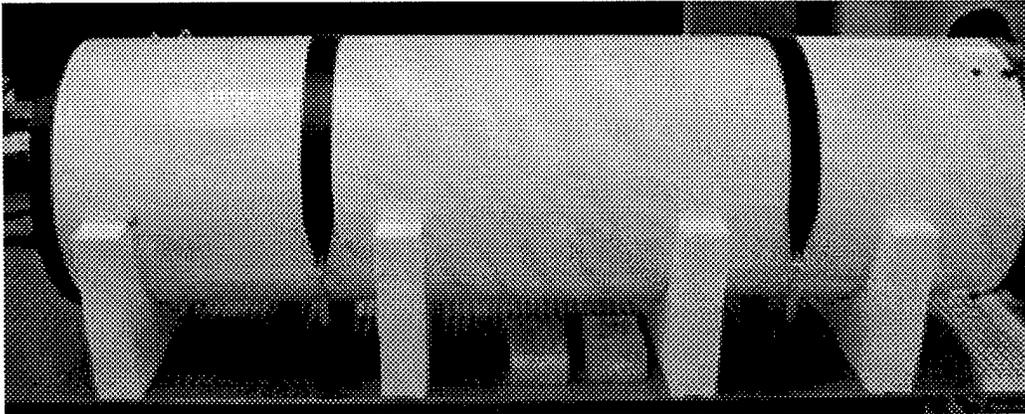
Figure 3.2: Technique for mounting the telescope on the optical bench. The Styrofoam supports are the original packaging material for the telescope, and the black straps are made for mounting the telescope to the base. Tension in the straps is adjustable, and effectively immobilizes the telescope.

can image sources placed down the hall at distances ranging from 7 to 15 meters, and rotated so that the light reflected by the secondary mirror comes out of the telescope parallel to the optical bench surface. The telescope is supported by four semicircular Styrofoam holders, and is fastened to the optical bench using two Meade straps intended for mounting the telescope on the base. The mounting technique can be seen in Figure 3.2. Once fastened to the table the telescope is immobilized and cannot rotate in any direction.

The numerical aperture (NA) of a telescope with a focal length f, and a mirror diameter D, is defined by the equation

$$NA = 0.5 \tan^{-1}\left(\frac{D}{f}\right) \tag{1}$$

The physical meaning of the NA for a telescope can be seen in Figure 2.4. For our 10" Newtonian telescope, the numerical aperture is 0.109 radians, and this must be matched to the numerical aperture of the RSI. The NA of an RSI with a shear angle θ, operating at a wavelength λ, and with a pixel size of Δ on the CCD is given by the equation [11]

$$NA = \frac{\lambda}{\Delta \sin \theta} \qquad (2)$$

A typical value for the RSI numerical aperture at a shear angle of 30° is 0.14 rad. Clearly, this NA is dependent on the shear angle θ, and so the optics designed to match the numerical aperture must be adjustable. In addition to matching the numerical aperture, the spot size at the CCD cannot exceed the size of the array, and the Fourier transform plane of the image must occur at the CCD as described in Chapter 2.

As mentioned before, the light collected from the telescope is reflected by the secondary mirror and exits the telescope parallel to the optical bench. A second flat mirror then reflects the light so that it runs parallel to both the optical bench and the axis of the telescope. This flat mirror is mounted using a magnetic base, and is placed close to the focal point of the 10" mirror so it can have a small diameter. After the two reflections by flat mirrors, light collected from the 10" mirror passes through two lenses designed to match the numerical aperture of the RSI and telescope. These lenses are placed on optical rails so that they are adjustable depending on the shear angle of the RSI. Both lenses are 2" diameter optics, and have focal lengths of 9 cm and 15 cm.

2.2. Rotational Shear Interferometer (RSI) Design

After passing through the two lenses, the numerical aperture of the RSI has been matched to the telescope. Light from the telescope now enters the RSI. The RSI is composed of a beam splitter and two right angle mirrors, all of which are 1" diameter optics purchased from Melles Griot. Figure 3.3 shows the physical design of the portable RSI. There is an anti-reflection coating on the beam splitter. The two right angle mirrors are anti-reflection coated on the hypotenuse and aluminum coated on the legs [4]. The mechanical mount of the RSI was designed by Ron Stack, Jason Gallicchio, and Chuck
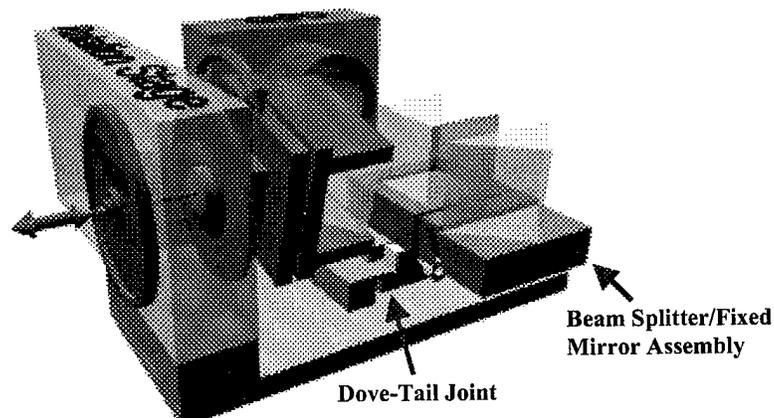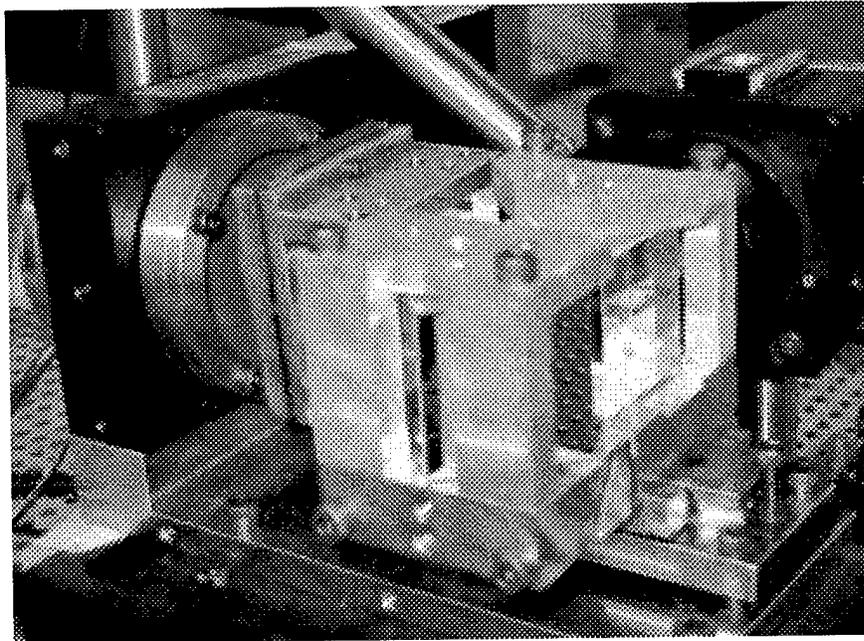
Figure 3.3: The RSI assembly. The piezo-stage and the rotating mirror are on the left of the image. The CCD is at the rear of the image. The beam splitter/fixed mirror assembly slides along the dove-tail joint. Bottom image taken from Gallicchio [4].

Henderson [4]. It is made out of Invar for thermal stability and was machined at the

University of Illinois at Urbana-Champaign. The shear angle of the RSI is controlled by a

Newport PR50PP rotation stage, which has an accuracy of 0.010 degrees [4]. A Piezo-

Electric disk translator, Physik Instrumente part P-286.40 [4] controls the optical path

delay. For more on the design of the portable RSI, please refer to Gallicchio's Masters Thesis [4]. The piezo-electric stage and the rotation stage are controlled by circuit boards mounted separately from the RSI. Both the computer and the operator have control over the optical path delay using the piezo-electric stage. The operator can change the shear angle of the rotation stage using two buttons mounted on the rotation stage's stepper motor circuit board. The computer cannot currently control the shear angle of the RSI, although that will change in the future.

The RSI rests on a lab jack so that it can be adjusted vertically. After passing through the matching optics, light enters the RSI and is divided by the beam splitter. The beams travel down the arms of the RSI, are reflected by the right angle mirrors, and recombine at the beam splitter. The RSI-produced fringes pass through a filter to make the light quasi-monochromatic before being projected onto the CCD camera. The filter used is manufactured by Melles Griot, and passes a 12 nm band centered around $\lambda = 646$ nm. The spectrum of the filter can be seen in Figure 3.4. Under the quasi-monochromatic assumption, every source has the same wavelength and there is no spectral/spatial degeneracy in the images produced by the RSI. Therefore, the FFTs obtained from the fringe pattern will preserve the spatial relationship of the light source.

The CCD camera has a 320×240 pixel array. Fringe patterns captured by the CCD camera are fed into a Dell computer loaded with Imagekitchen software. Imagekitchen performs all of the analysis on the fringe patterns including Fast Fourier Transforms (FFT) and wavelength filtering. It also controls the piezo-electric stage. Due to the nature of the FFT, only a 128×128 block of pixels can be used from the CCD. The

Red Filter Spectrum
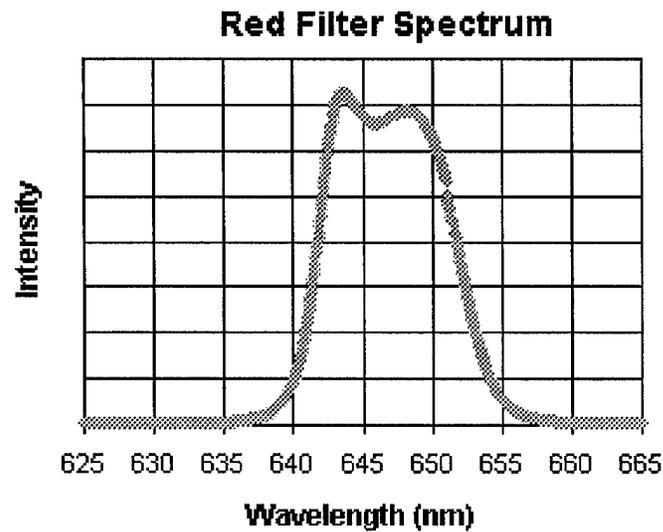
Figure 3.4: Spectrum for the red filter used in the experiments. The filter was used when imaging the incoherent white fiber light.

block of pixels is selected depending on the quality and placement of the fringes on the CCD as viewed by the operator on the monitor.

2.3. Light Sources

There have been multiple sources used with the RSI/telescope combination. As mentioned above, the telescope rests on an optical bench and is directed down a short hallway in the laboratory area. For a given experiment, the source ranges from 7 to 15 meters from the telescope aperture. This experiment has dealt primarily with white fiber light sources and quasi-monochromatic light emitting diodes (LEDs) of varying colors. The fiber light is composed of a very bright white light bulb inside a case. Light from the bulb is coupled into a 1 cm diameter optical fiber. The fiber extends from the case and can be turned and held in any direction. The intensity of the fiber light is controlled using a dial on the case. Light from the fiber light is not collimated. Since the focal length of the telescope is the length at which collimated light is focused, the 10" mirror does not focus light from the fiber light at 45". This changes the effective NA of the telescope.

Red/Yellow/Green LED Spectra
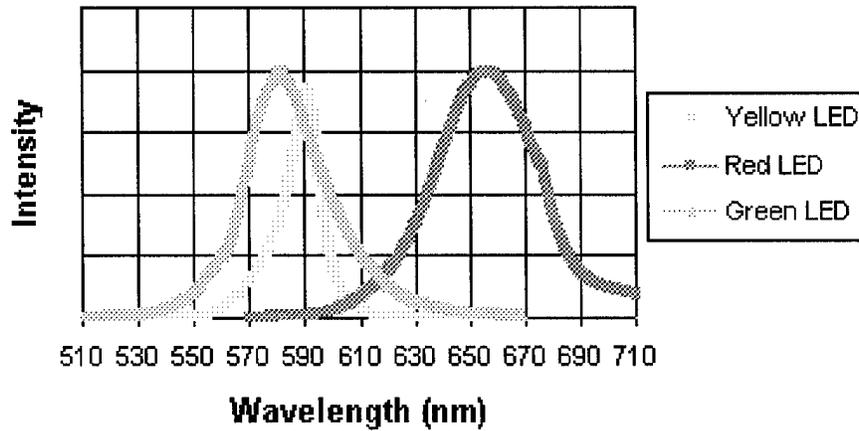
Figure 3.5: Spectral data for the three LEDs used in the experiment. The voltage drop across each LED is 3V. Experiments included red/red, red/green, and red/yellow pairing. The green/yellow pairing was never used due to the similarity in wavelength.

The Mathematica code designed to match the NA of the telescope to the RSI must be altered slightly to handle non-collimated light properly, but the calculation is straightforward and is demonstrated later in this Chapter.

The other main source used is the light emitting diode (LED). The LEDs used operate at a peak wavelength of $\lambda = 655\,\text{nm}$ (red), $\lambda = 590\,\text{nm}$ (yellow), or $\lambda = 580\,\text{nm}$ (green). The spectra for each LED can be found in Figure 3.5. Each one is 0.5 cm in diameter and emits quasi-monochromatic light so the filter is removed from in front of the CCD. The LEDs are plugged into a breadboard and powered by a 10V source. The voltage drop across the LEDs is typically 3V. The breadboard is mounted vertically so that the LEDs are directed towards the telescope. The LEDs are also not collimated sources, so an appropriate adjustment is made to the NA matching code. The quasi-monochromatic nature of the LEDs makes it possible to use multiple LEDs and image multiple wavelengths at once. However, the LEDs are not as bright as the fiber light

source and the massive photon loss of the system (discussed in Chapter 5) makes it difficult to image the dim fringe pattern generated by the RSI.

The HeNe laser has also been used as a source for alignment purposes. The HeNe is placed at the end of the hallway about 15 meters away from the telescope aperture. Immediately after exiting the laser, the beam is passed through a spatial filter and then collimated to create a temporally and spatially coherent plane wave. The 10" mirror focuses this beam at 46", meaning that the collimation of the beam is not perfect. By shifting the collimating optics the laser source can either be used as a collimated beam, or it can be made into a diverging beam that fills the 10" mirror. For this experiment Imagekitchen took no fringe pattern images of the HeNe laser. Previously, Gallicchio used the RSI to image a point of laser light on a rotating diffuser to eliminate speckle. The results can be seen in his Masters Thesis [4].

3. Experimental Procedure

3.1. Optical Alignment

3.1.1. RSI Alignment

To begin RSI alignment, the beam splitter and fixed right angle mirror assembly is removed from the instrument. A laser is mounted on the optical bench so that it is directed into the center of the rotating right angle mirror. The laser should remain centered on the back right angle of the mirror as it rotates around. The rotating mirror must be adjusted so that it reflects the laser light back into the laser aperture for every rotation angle. To accomplish this both the tilt of the rotation axis of the RSI and the tilt of the right angle mirror with respect to the rotation axis must be adjusted. First align the

rotation axis of the RSI with respect to the laser. If the retroreflection off the right angle mirror is above the laser aperture during rotation, slips of lens paper are inserted to tilt the rotation axis down. If the retroreflection is off to one side of the laser, the RSI itself is rotated[4]. Once the retroreflection makes a circle around the laser aperture during the rotation of the right angle mirror the tilt of the mirror with respect to the rotation axis is adjusted. There are screws on the prism mount to change the tilt, and after each mirror adjustment the laser must be tuned to keep it in the center of the mirror during rotation. When the alignment of the rotating mirror is correct the mirror will reflect the laser into itself through 360° rotation [4].

The next step is to align the beam splitter and fixed right angle mirror. The alignment procedure that follows is taken from Gallicchio's Thesis [4]. First, the aligned rotating mirror is blocked with a slip of paper. Then the beam splitter/fixed mirror assembly is slid onto the dove-tail joint. The beam splitter is placed on the assembly and rotated it until the retroreflection off the anti-reflection coating lies above or below the laser aperture. The vertical tilt can be adjusted using screws on the assembly itself, after the beam splitter is locked into position with the screws on top of the assembly. The adjustment screws on the assembly are used to direct the reflection off the beam splitter back into the laser aperture [4]. With the beam splitter aligned, the fixed mirror is slid onto the assembly so that the laser is centered at the back right angle. This mirror is rotated until the reflection off the anti-reflection coating goes back into the laser aperture, and then the mirror is locked down using the screws from above [4].

Now the rotating mirror, the fixed mirror and the beam splitter are aligned with each other and with the laser. Next the beam splitter/fixed mirror assembly is translated

along the rail until the path lengths of the two arms are identical. To do this, the adjustment screws on the dove-tail joint are loosened so that the beam splitter/fixed mirror assembly slides along the rail. Set the piezo-electric translator on the rotating mirror to the middle of its range using the control box dial. Since there is no micrometer on the instrument to fine-tune the position of the beam splitter/fixed mirror assembly along the rail one must be created externally, otherwise the alignment must be done by hand. Place a micrometer on the optical bench directly in front of the RSI. Using posts found in the lab, construct a small arm on top of the micrometer to push the assembly along the rail. The arm must be constructed so that it does not block light from entering the RSI and it pushes the beam splitter/fixed mirror assembly along the rail without rotating it. The arm is adjusted correctly if the reflections off the beam splitter and fixed mirror return to the laser aperture as the assembly is pushed along the rail. The micrometer will help in the adjustment of the optical path lengths.

At the point where the path lengths between the two arms are the same, the RSI generates fringes for incoherent white light. Laser light is temporally coherent, so fringes will occur at any path length difference and it cannot be used to align the RSI path lengths. The laser is removed and replaced with a white light source. An iris is then placed in front of the white light source, and a pin is taped to the iris so that the point is on the optical axis of the RSI. The CCD camera is mounted on the optical bench so that it is directed at the beam splitter, and focused on the pin. With the shear angle at 0°, the images of the pin from the rotating and fixed mirrors should lie directly on top of one another. Finally, the micrometer is used to translate the assembly along the optical rail until white light fringes appear. This can take several hours. When the path lengths are
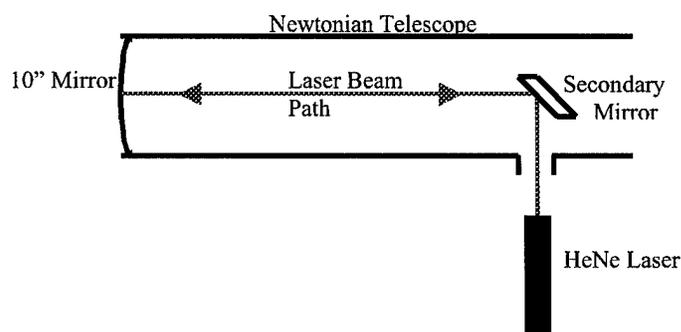
Figure 3.6: Laser placement for telescope rotation alignment. The HeNe laser was used to ensure the beam reflected by the secondary exited the telescope parallel to the optical bench.

equal, the sides will form a line, as can be seen in Figure 2.2, and this is used as a guide to align the path lengths. When the path lengths are equal and the RSI produces fringes, the assembly is carefully locked down by tightening the adjustment screws a little bit one at a time so that the fringes are not lost. After the assembly is locked down, the RSI is aligned and is ready to measure spatial and temporal coherence.

3.1.2. Source/Telescope Alignment

With the RSI producing fringes, the most difficult part of the alignment is finished. The next step is aligning the telescope and the source. The telescope is mounted on the optical bench so that it has at least 7 meters of open space in front of it, and rotated so that the secondary mirror reflects the light off roughly parallel to the optical bench. A HeNe laser is used to fine-tune the rotation of the telescope. The HeNe laser is mounted to the side of the telescope as can be seen in Figure 3.6, so that the laser beam is parallel to the optical bench and is directed into the center of the secondary mirror. The beam from the laser is reflected by the secondary onto the center of the 10" mirror. The 10" mirror then reflects the beam onto the secondary and out of the telescope tube. The telescope is aligned properly when the laser beam coming out of the telescope travels along the path of the beam going into the telescope. The telescope tube is rotated

until the two paths are the same, and then it is locked down using the mounting straps shown in Figure 3.2. Now the beam exiting the telescope is parallel to the optical bench, and the telescope is aligned properly.

The source is placed on a bench about 7 meters away from the telescope aperture. The light exiting the telescope must run parallel to the optical bench for it to couple into the RSI properly. Since the lab light sources do not emit plane waves, the orientation of the source with respect to the telescope optical axis matters. For example, if the source is 8 m from the telescope, and 5 cm off the optical axis then the telescope mirror will focus the source at 133.3 cm (52.5 in) and -.833 cm off the optical axis. The Mathematica calculations for this example can be found in Appendix B. If the focus of the image is not on the optical axis of the RSI/telescope combination, then the beam is not parallel to the optical bench. Therefore, the source must be on the optical axis of the telescope for the focused image to be on the optical axis. To make sure that the source is on the optical axis of the telescope look at the doughnut pattern of light exiting the side of the telescope. Adjust the source until the secondary mirror blocks the exact center of the collected light. At this point the source lies on the optical axis of the telescope and the source is aligned properly.

3.1.3. Matching Optics Alignment

The light collected by the telescope is now exiting the side of the telescope parallel to the optical bench. Two lenses are used to match the numerical aperture of the telescope to that of the RSI. A flat mirror is placed close to the focal point of the 10" mirror to reflect the telescope light so that it runs parallel to both the optical bench and the optical axis of the telescope. An optical rail is mounted on the optical bench and an

iris is placed on the rail. The height of the iris is adjusted until the center is on the optical axis. As the iris moves along the rail, it should always block the very center of the telescope beam. If this is not the case, the position and tilt of the flat mirror are changed until the beam from the telescope is directed along the rail. Now the two lenses are placed on the rail, and the height is adjusted so that their center is on the optical axis. These lenses will match the NA of the telescope to that of the RSI.

For the laboratory proof of concept phase of the RSI/telescope combination experiment several approximations were made for the NA matching. First, as discussed before, the sources in the lab do not produce collimated light. The telescope focuses collimated light at a distance of 45". However, for the sources in the lab the effective focal length of the mirror, due to the divergence in the source beam, was typically 48". The NA matching code has no problems dealing with this situation. The problem can be solved by substituting the effective focal length of the mirror for the actual focal length of the mirror. For the code, this approximates the diverging source as a collimated source that is focused by a mirror with a focal length greater than 45". Some of the light collected by the telescope misses the secondary mirror and is reflected and focused out the front of the telescope tube. The effective focal length of the mirror is calculated by measuring the distance of the focal point away from the end of the tube and adding 42". Also, for the proof of concept phase of the experiment, the RSI shear angle was changed frequently. To avoid moving the lenses for each different shear angle, the light from the telescope was collimated before entering the RSI. Thus, the lens placement did not shift with changes to the shear angle, and the NA of the telescope and the RSI were never exactly matched for the experiment. Later versions of the experiment will exhibit full

NA matching, but for the proof of concept phase the main concern was spot size on the CCD and not input angle.

Lens placement distances for the NA matching were calculated with a Mathematica code using geometrical optics, which can be found in Appendix A. The code, titled *abcd numerical aperture*, takes as inputs the focal length of the mirror, the focal lengths of the two lenses, the initial position and trajectory of the ray to be traced through the system, a restriction on the final position of the ray, and a total distance restriction for the matching optics system. As mentioned above, for this experiment the effective focal length of the mirror was entered as the actual focal length of the mirror. The lens combination used was either two 9 cm lenses, or one 9 cm lens and one 15 cm lens. All lenses were 2" diameter optics. The ray traced through the system started off at an initial position of 5" off the optical axis, and an initial angle of 0°. These values correspond to collimated light captured by the outer edge of the telescope mirror. The final position of the ray off the optical axis must be smaller than the CCD array size, so the value was 0.2 inches. The final angle of the ray with respect to the optical axis was 0°, as explained above. The total distance restriction was 80" from the telescope mirror to the CCD screen. Eventually the RSI and matching optics will form a portable instrument, and the distance restriction ensures the instrument size is small. With these inputs, the Mathematica code calculated the lens placement distances. One last constraint on the system is that the beam never expands to a size larger than the 2" lenses. The end of the code uses the distance values calculated to find the size of the beam as it passes through each lens. If the beam size stays less than 1" off the optical axis, and the distances are positive, then the calculation is successful.

Once the lenses are at the proper height, they are mounted along the optical rail at the distances calculated by the Mathematica program. The height of the RSI is adjusted using a lab jack so that the light from the second lens goes through the interferometer and onto the CCD camera. When the lenses are placed properly there is an image of the doughnut pattern on the CCD camera, and the spot size is smaller than the 320×240 array. With the optics properly aligned, it is possible to measure the spatial coherence of the source using the RSI and generate an image through computer-based Fourier analysis.

3.2. Capturing and Analyzing Images

Before taking any images, the shear angle on the RSI must be adjusted. With the light source turned on, and with all of the optics aligned properly there should be a fringe pattern on the CCD screen. The buttons on the stepper motor controller change the shear angle of the rotation stage. As the shear angle increases the points on the wavefront being interfered get further and further apart. With increasing shear angle the spatial coherence between interfering points gets smaller, and the fringes get closer and closer together. A shear angle is chosen in the middle of the range where there is good fringe visibility on the CCD. Usually the shear angle is set between 5° and 20°. Now the image generating process is ready to begin.

To start the image-taking process, the Imagekitchen software on the computer is opened, and the script *autocorrelate* is loaded. The code for the *autocorrelate* function can be found in Appendix C. With the source on, the filter in place (for white light sources), and all of the optics aligned, there is a fringe pattern on the CCD. The fringes are contained in the doughnut pattern produced by the telescope mirror and secondary. Thus the fringes do not cover the entire CCD screen. There will be a region where the

fringe pattern has particularly good contrast. To initialize the *autocorrelate* function, the operator estimates a pixel value in the region of good fringe visibility. This pixel value is entered into the variables "pointx" for the x component, and "pointy" for the y component. The *autocorrelate* script is then run. *Autocorrelate* dithers one arm of the RSI through 64 optical path length differences using the piezo-electric translator. As the path length of one arm is changed with respect to the stationary arm, the phase between the two interfering waves changes. The change in phase results in the movement of fringes on the CCD screen. Through the 64 dithering steps, an individual fringe moves approximately 8 wavelengths away from its initial position. At each dithering step the program captures a fringe pattern from the CCD. The script then takes the pixel value at (pointx, pointy), plots it as a function of the optical path length. For good fringe contrast, the pixel value vs. path length plot looks sinusoidal. The *autocorrelate* function then calculates the wavelength of the fringes based on the sinusoidal wave. The resulting wavelength is not given in nanometers, but in a length scale based on the voltage applied to the piezo-stage. This wavelength value is used in the image-taking code.

Image collection is done using the *telescopealtend2* script in <u>Imagekitchen</u>. The code for the *telescopealtend2* script can be found in Appendix D. The wavelength found by the *autocorrelate* function is entered into the variable named "cwave." Typical values for "cwave" are 273 for the red filtered fiber light, and 195 for a blue led (these are not nm, length is based on piezo-stage voltages). Although the CCD screen is 320×240 pixels, only a 128×128 block of the array is used for imaging. This is a result of the FFT performed on the fringe pattern. The FFT function assumes that the fringe pattern being analyzed is a square of pixels with sides of length 2^n pixels, where n=1,2,3.... Therefore
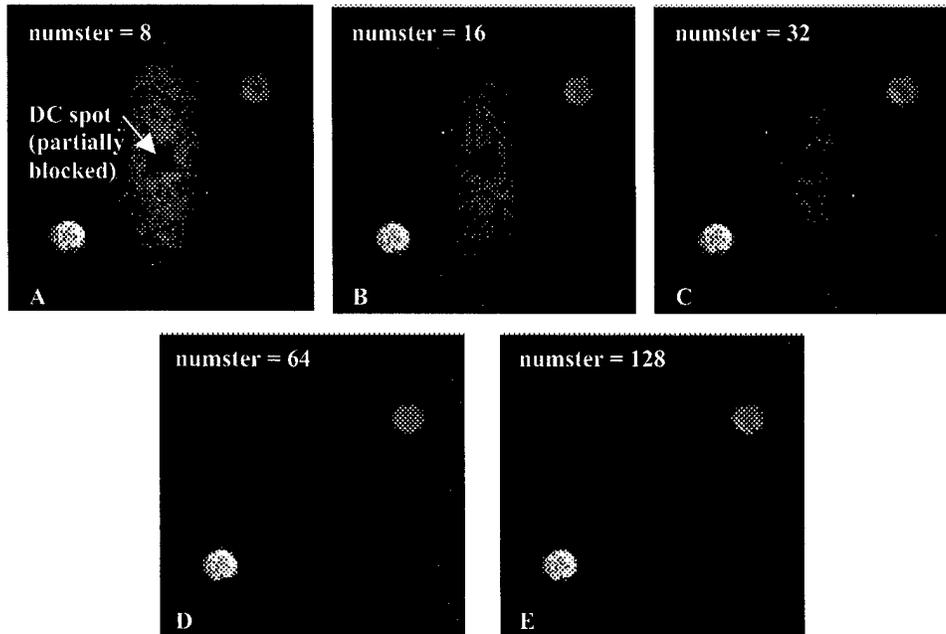
Figure 3.7: The effects of a change in the number of dithering steps are shown in this series of FFT images of the source. The source was a fiber light with a protractor placed with the number 20 in contact with the end of the fiber. The red filter was used to enforce the quasi-monochromatic assumption. The cumulative fringe pattern of which image A is the FFT contained 8 dithering steps. The cumulative fringe pattern corresponding the image E contained 128 dithering steps. The dithering range (i.e. the total distance the piezo-stage covered during fringe pattern collection) was the same for each value of "numster." Note that as the number of dithering steps, and thus the sampling rate of the dithering range, increased the DC spot decreased in intensity. The wavelength filtering effect increases in effectiveness as the value of "numster" increases. Notice also that the backwards 20 slightly increases in clarity as "numster" increases. There are two images of the source due to the positive and negative frequencies in the FFT.

the maximum size of the fringe frame available on a 320×240 pixel CCD is 128×128.

The operator finds a 128×128 box with particularly good fringe contrast on the monitor, and then estimates the position of the upper left hand pixel. This pixel value is entered into the variables "sp_begx" and "sp_begy." Typically, the 128×128 box of pixels contains a quarter of the doughnut image from the telescope.

Another variable which is changed quite often is the "numster" variable. This variable controls the number of dithering steps the telescope script takes while building up an image. Typically its value is set to 32, but it can be as low as 8 and as high as 128.

The changes in FFT image quality based on the value of "numster" can be seen in Figure 3.7. The *telescopealtend2* script is now ready to run.

When the *telescopealtend2* script runs, it dithers one arm of the RSI through "numster" optical path length differences. At each path length difference the script captures a fringe image. As mentioned before, the result of a dithering step is a slight shift in the position of the fringes on the CCD screen. In an interferometer, dithering one of the arms is used to calculate the spectrum of the source. For the RSI experiments performed in the proof of concept phase of the project, no spectral information was collected. The dithering performed by the *telescopealtend2* code is for a different purpose. The imaging script uses the optical path length dithering to filter out the features of the CCD image that do not change with the same or similar wavelength to the "cwave" variable. This is accomplished through the use of phasors. Each individual fringe image taken by the CCD is a 128×128 array of pixels. Consider one pixel at position (x,y) on the CCD screen. The *telescopealtend2* imaging script finds the pixel value at (x,y) in the cumulative fringe pattern through the sum

$$p_c(x,y) = \sum_j p_j(x,y) \exp[i\phi_j] \tag{3}$$

where $\phi_j = \dfrac{2\pi}{\lambda} \dfrac{n_j d_j}{N}$ is the expression for the phase. In these equations $p_c(x,y)$ is the cumulative pixel value, $p_j(x,y)$ is the pixel value at (x,y) in the jth fringe image, $i = \sqrt{-1}$, λ is the input wavelength "cwave," N is the total number of steps "numster," and n_j and d_j are the jth step number and dithering distance, respectively. Thus each pixel in the frame is multiplied by a phase term and summed together to generate a

49
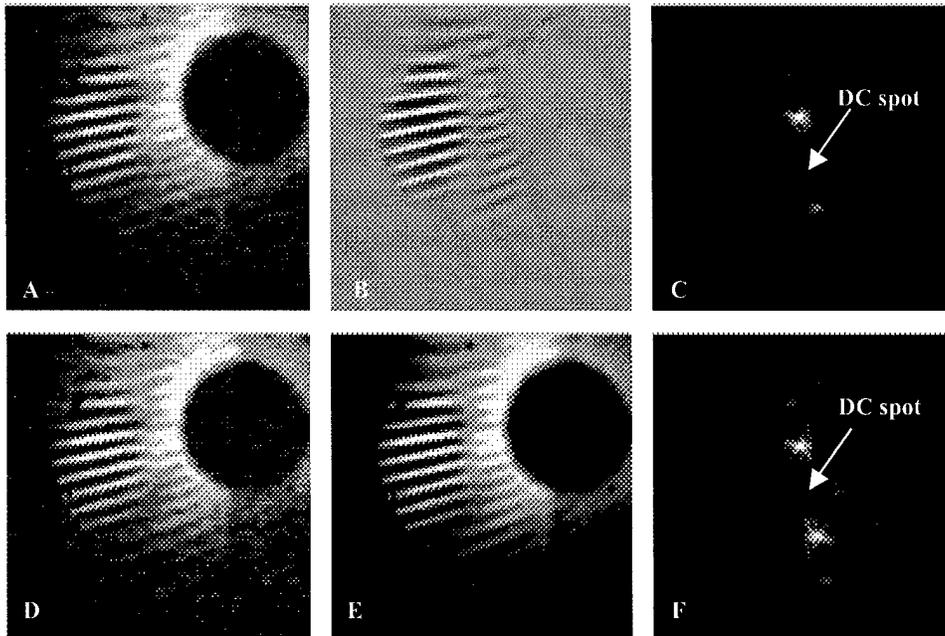
Figure 3.8: The effects of phasor wavelength filtering. For this experiment the total number of fringe images added together was "numster=32." Images A, B, and C were taken with the phase term included in the code. Images D, E, and F were taken without the phase term included. Images A and D are individual fringe patterns captured by the CCD. Images B and E are the cumulative fringe patterns calculated by *telescopealtend2* for each case. Images C and F are the FFTs of images B and E, respectively. Notice that the individual fringe images for the two cases, A and D, are identical. However, the phase term creates radically different cumulative fringe patterns. In image B, all of the pixels that do not contain some portion of the fringe pattern were reduced to zero by the phasor multiplication. This virtually eliminated the extreme low frequency fringe of the telescope doughnut pattern, and removed the DC spot from the FFT image. In image E, without phasor multiplication, the low frequency doughnut pattern remains and creates a large DC spot in the FFT image. The DC spot has been partially manually blocked by a group of zero-value pixels. The source is a white fiber light, and the light was filtered using the red filter. There are two points corresponding to the source in the FFT images C and F due to the positive and negative frequencies in the FFT. All images are 128×128 pixel arrays.

complex final pixel value. The cumulative fringe image must contain real pixel values, so the real portion of each pixel value is retained to form the fringe image.

These phasors produce a rudimentary wavelength filtering effect. When one arm of the interferometer dithers, the fringes shift on the CCD array. The wavelength used to calculate the phase ϕ_j is the value determined by the *autocorrelate* function. Phasor multiplication leaves all the fringes that shift with the determined wavelength in the cumulative fringe image, and cancels out those fringes with a different wavelength.

When the wavelength of a fringe is close to the "cwave" value, the phasor multiplication leaves the final pixel value unchanged from the first individual fringe pattern. However, when the wavelength is significantly different from the "cwave" value, the phasor multiplication averages the pixels in the fringe pattern to something much less than the original pixel value, thus eliminating them from the cumulative fringe pattern. Luckily the filtering is not particularly sensitive to slight changes in the value of "cwave." This made it possible to image red and green LEDs simultaneously. The effectiveness of the phasor wavelength filtering can be seen in Figure 3.8.

In this way the *telescopealtend2* code builds up a cumulative fringe pattern. The FFT of the fringe pattern gives an image of the source. For the 128×128 cumulative fringe pattern, the FFT produces a 128×128 plot of the image. The 128×128 cumulative fringe image can be expanded using an operation known as zero-padding. The *telescopealtend2* code zero-pads the 128×128 cumulative fringe pattern out to a 512×512 image. This is done by creating a 512×512 image with zero for every pixel value. The 128×128 cumulative fringe image is added to the upper left hand corner of the 512×512 zero image. The FFT of the 512×512 zero-padded image looks identical to the FFT of the 128×128 cumulative fringe pattern because no information is added. The only difference is that the FFT image is blown up to a 512×512 array of pixels.

An important feature of each FFT plot is the DC spot. The DC spot comes from the constant term in the Fourier transform [4]. It appears in the center of the two-dimensional FFT plot. Since the DC spot contains no information about the source it is blocked from the image by a small array of zero-valued pixels of width "width1" for the 512×512 FFT plot, and "width2" for the 128×128 FFT plot. When calculating radial

shifts due to wavelength in Chapter 5 the DC spot is used as the origin of the FFT plot. When there are extremely low frequency fringes in the cumulative fringe image, such as the doughnut pattern of the telescope, the DC spot can expand beyond the blocking array of pixels. These effects can be seen in Figures 3.8 and 3.7.

The output of the *telescopealtend2* script consists of the cumulative fringe pattern, the first individual fringe pattern, the zero-padded fringe pattern, and the 128×128 and 512×512 FFT plots. The FFT plots are images of the source, and are the final goal of the imaging system.

CHAPTER 4
DATA COLLECTION TECHNIQUES

1. Experiments Performed

The long-term goal of the RSI/telescope project is to attach an RSI instrument to the Three College Observatory (TCO) telescope to image a previously unresolvable binary star and demonstrate atmospheric correction. With this goal in mind, the objective of the proof of concept phase of the experiment was to exhibit these abilities in the lab, and to make sure that the images gathered using the RSI/telescope combination fit with theory. Our group performed a series of four experiments on a synthetic binary star constructed out of LEDs to test the RSI/telescope combination. The first experiment used a synthetic binary made of two identical red LEDs with varying angular separation at a low shear angle. The second experiment used the same synthetic binary and varying separation with an increased RSI shear angle. The third experiment tested the RSI's sensitivity to wavelength changes by imaging two identical red LEDs, and then replacing one of the red LEDs with a green LED in the same position. The shift of the green LED's FFT point relative to the red LED's FFT point shows the sensitivity of the RSI to wavelength changes, and is proportional to the change in wavelength. Finally, to test the RSI's ability to handle atmospheric distortion, a hot plate was placed just below a

synthetic binary of identical red LEDs. The hot plate varied in temperature from 150 C to 300 C, and the binary was imaged through the resulting turbulence. The changes listed above were the only alterations made to the experimental setup between experiments. All parameters in the imaging computer code, and the alignment of the RSI/telescope combination were untouched during the data taking process.

2. Data Collection Setup

2.1. Computer Code Parameters

The Imagekitchen code titled *telescopealtend2* performed all data collection and image generation. The *telescopealtend2* code can be found in Appendix D. Once set, the variable values in the *telescopealtend2* code were unchanged throughout the data collection process. What follows is a breakdown of each significant variable value in the *telescopealtend2* code. The first major variable is "cwave." As discussed in Chapter 3, the "cwave" variable is determined using the *autocorrelate* function in Imagekitchen. The "cwave" variable measures the distance that the piezo-stage steps through to register one full wavelength shift in the fringe pattern. For the data collection, "cwave=320," which is a typical value for a red source (and is *not* in nm). The "numwaves" variable determines the total number of wavelengths the piezo-stage steps through when generating an image. For the data collection process "numwaves=1," so the piezo-stage only stepped through one full wavelength to generate the final fringe pattern. The "cwave" and "numwaves" variables combine to calculate the total dithering distance of the piezo-stage during image collection. The calculation is dithwidth=(cwave/2)*numwaves, and then startdith=middith-dithwidth and enddith=middith+dithwidth where "middith" is the

middle of the dithering range determined by the operator. For this experiment, "middith=18000," which is a value specific to the piezo-stage on the RSI.

The variables "width1" and "width2" were set to "width1=21" and "width2=11." These variables determine the size of the box used to block the DC spot from the center of the FFT image. The "width1" variable controls the size of the box for the 512×512 zero-padded FFT image, and the "width2" variable controls the size of the box for the 128×128 FFT image. These sizes are set to be much larger than the actual DC spot to assure that the spot is totally cut out of the FFT frame. The total number of dithering steps is set by the variable "numster," and in this case "numster=32." This means that the *telescopealtend2* code took 32 fringe pattern images, each at a different dithering distance, to generate the final fringe pattern. This value of "numster" was chosen to provide effective wavelength filtering in a reasonable amount of time. For Imagekitchen to take 32 fringe pattern images, it typically takes 5 minutes. Each of the 32 fringe patterns is multiplied with a phase factor, determined by the current dithering distance and the variable "cwave," and added to the cumulative fringe pattern image (the process is described in Chapter 3). This creates the wavelength filtering effect.

2.2. Source Alignment

For the data collection process, all of the optics, from the telescope to the RSI, were aligned as described in Chapter 3. The synthetic binary star consisted of a pair of LEDs placed on a breadboard in parallel, and in series with a resistor. The breadboard circuit was connected to a power source, and the voltage drop across the LEDs was 3V. This synthetic binary was placed 8.7 meters away from the telescope mirror along the optical axis of the telescope and the RSI. The breadboard was mounted so that the tops
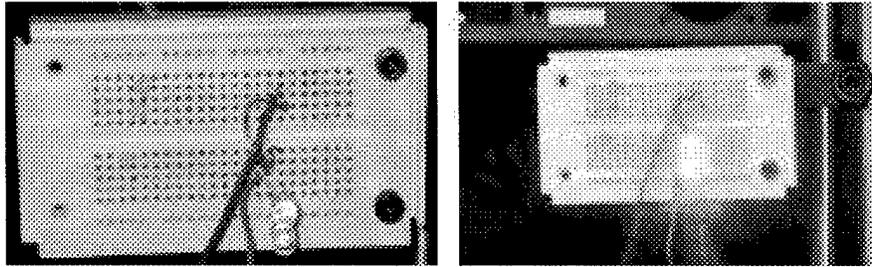
Figure 4.1: Two red LEDs mounted on a breadboard. The tops of the LEDs point towards the telescope. The separation of the synthetic binary was controlled by the holes on the breadboard.

Red and Green LED Spectra
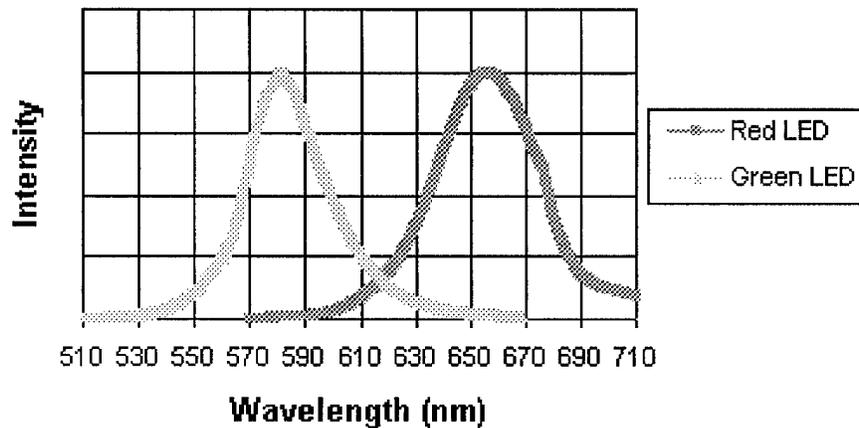
Figure 4.2: The spectra for the red and green LEDs used in the final experiments.

of the LEDs were directed toward the telescope aperture, as can be seen in Figure 4.1.

The separation of the LEDs was controlled by shifting one LED between holes on the

breadboard while keeping the other LED's position constant. This allowed for

separations of 0.7 cm, 1.0 cm, 1.3 cm and 1.6 cm. The spectra for the red and green

LEDs can be seen in Figure 4.2. The LEDs were purchased at Radio Shack. For the

fourth experiment involving atmospheric turbulence, a hot plate was placed just below

the level of the LEDs, as can be seen in Figure 4.3. The hot plate temperature varied

between 150 C and 300 C. At each temperature level a synthetic binary star with two

identical red LEDs at a separation of 0.7 cm was imaged by the RSI/telescope
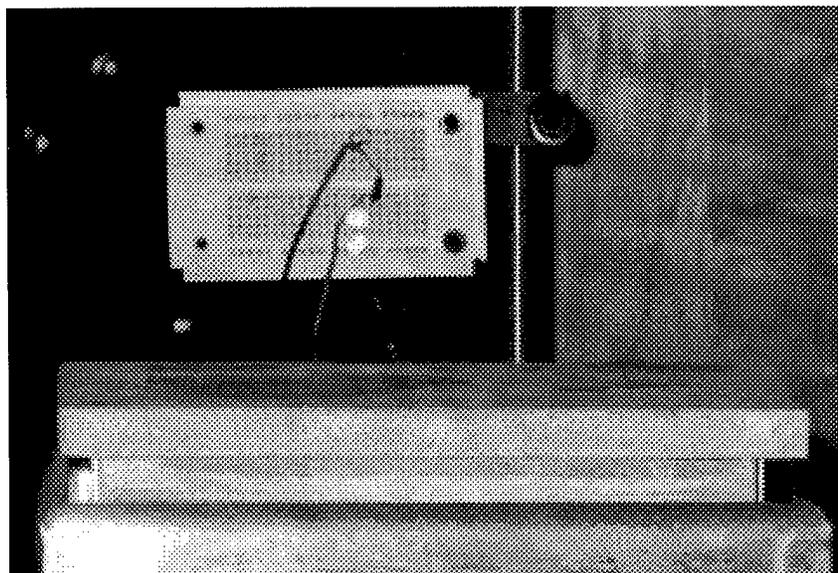
Figure 4.3: Hot plate placement relative to the synthetic binary source. The hot plate is ~6 inches in front of the synthetic binary, and ~1 inch below. The hot plate temperature varied between 150 C and 300 C.

combination. Convection waves from the hot plate distorted the wave front of the LEDs before entering the telescope and led to fringe movement on the CCD screen.

Although the LEDs are directional sources, their peak emission is not directly out of the top of the LED. The LEDs had to be pointed slightly off axis so that the peak light emission entered the telescope aperture. When the LEDs were pointed directly at the telescope, the RSI fringe pattern was not strong enough to register on the CCD camera, but when the LEDs were pointed slightly off axis there was enough light to capture fringe patterns.

3. Data Collection Procedure

The experimental setup is now ready to take data. First the operator needs to turn off the lights in the room. The data collection process begins by pressing the "Run Script" button in Imagekitchen. This starts the *telescopealtend2* code that collects the images. As described in Chapter 3, the code takes a series of raw fringe pattern images,

combines them with phasor terms, and generates a cumulative fringe pattern. Then the cumulative fringe pattern is passed through an FFT and the resulting transform plot is an image of the source. During image collection the system is entirely automated. The operator's only task is to stay out from in front of the telescope, and make sure that the lights are not turned on during the experiment. When the image collection is finished there are five images on the Imagekitchen screen: a raw fringe image, the cumulative fringe image, the zero-padded fringe image, the FFT of the cumulative fringe image, and the FFT of the zero-padded fringe image. Each of the images must be saved into a separate file. The system is immediately ready to produce new images and requires no downtime or priming. Results and discussion of the experiments are found in Chapter 5.

CHAPTER 5
RESULTS AND ANALYSIS

1. Two Identical LEDs

1.1. Results and Analysis for Varied Spacing

The first synthetic binary star created for testing the RSI/telescope combination used two identical red LEDs of the type specified in the Chapter 4. The separation between the two LEDs was varied between 0.7 cm, 1.0 cm, 1.3 cm and 1.6 cm. At each separation the Imagekitchen software calculated a cumulative fringe pattern out of 32 individual images, and then performed an FFT to generate an image of the synthetic binary source. Figure 5.1 shows the difference between each of the steps in the Imagekitchen image generation. The wavelength filtering performed by the software does an excellent job of eliminating the doughnut pattern produced by the Newtonian telescope. When this filtering is not included in the software, the doughnut pattern enters the FFT and appears to be a low frequency fringe. This low frequency fringe then generates a large DC spot and degrades the quality of the FFT. What is left of the DC spot after the filtering is blocked from the FFT image as mentioned in Chapter 4.

In the experimental setup of the synthetic binary star, as can be seen in Figure 4.1, the red LEDs are oriented vertically in relation to each other. The vertical alignment
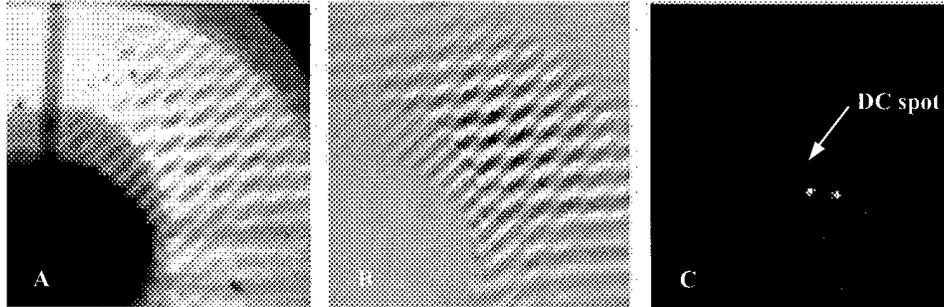
Figure 5.1: Two fringe patterns and an FFT image representative of experimental data. Image A is a raw fringe image as seen by the CCD camera without any filtering. Image B is the cumulative fringe pattern generated from 32 fringe patterns of type A, each multiplied with a phase factor. Notice that the doughnut pattern cancels out of the image, thus eliminating extremely low frequency fringes and the DC spot. Image C is the FFT of frame B, and recovers an image of the source. When present, the DC spot is in the center of the FFT image. These three images correspond to two identical red LEDs at a separation of .7 cm, placed 8.7 meters from the telescope mirror, and taken with a low shear angle. Since the LEDs have an identical wavelength the relative position of the LEDs is preserved in the FFT. Each image is 128×128 array of pixels.

translates into a horizontal alignment on the FFT plot, with the left point corresponding to the lower LED on the breadboard. The spacing between the LEDs is controlled by moving the upper LED up or down in relation to the stationary lower LED. The effect of the variable spacing can be seen in Figure 5.2. At each step, the spacing between the LEDs is increased by 0.3 cm. There is a linearly proportional change in the separation of the points on the FFT plot due to this change in spacing. Notice how the left FFT point stays stationary in each of the four images and that the shape of the point is nearly identical in all cases. This demonstrates the reproducibility of the imaging process, and that the changing fringe pattern for the upper LED does not affect the fringe pattern for the lower LED. The FFT software has no difficulty distinguishing the two fringe patterns.

The angular separation of the synthetic binary star varies from 165.7 arc-seconds for 0.7 cm of separation, to 379.4 arc-seconds for 1.6 cm of separation. As mentioned in Chapter 1, the resolution limit for a ground-based telescope without atmospheric compensation is about 1 arc-second. Although this is not near the resolution limit, it is
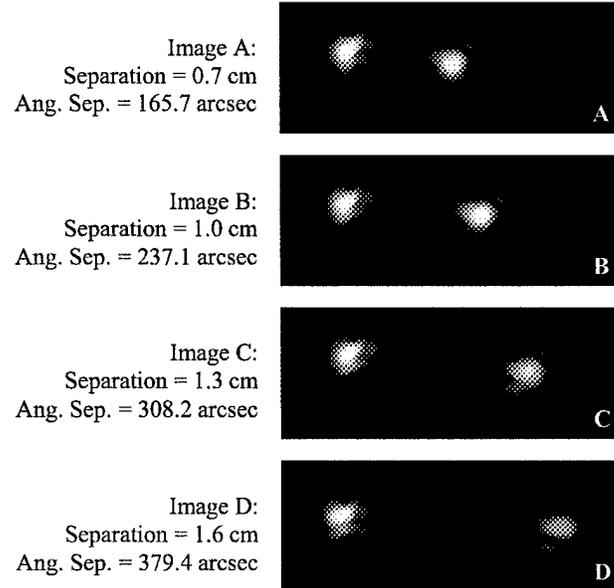
Figure 5.2: A comparison of FFT images for identical red LEDs with varying spacing. The LEDs are placed 8.7 meters from the telescope mirror, and vary from a separation of 0.7 cm in image A, to a separation of 1.6 cm in image D. The angular separation as seen by the telescope ranges from 165.7 arc-seconds to 379.4 arc-seconds. Note that the spacing on the FFT shifts linearly with changes in the physical spacing of the LEDs.

hoped that the RSI/telescope combination can image above the resolution limit for ground-based telescopes without atmospheric compensation.

The spectrum of the red LEDs used in this experiment is given in Figure 4.2, and although the LEDs peak in the red, the light emission bandwidth is large at approximately 80 nm. This large bandwidth accounts for 25 % of the visible light spectrum, and clearly is not monochromatic. For the LED experiments the light is not filtered before the CCD to enforce the quasi-monochromatic assumption. For a white light point source with equal emission at every visible wavelength the FFT would display a line pointing radially from the center of the plot. This line would contain information on the direction to the source, and the spectrum of the source. However, the FFT of the red LED fringe pattern still maps into a single point representing the LED's spatial position. This indicates that even with a bandwidth of 80 nm, the red LED still falls within the quasi-monochromatic

approximation for the RSI/telescope combination. As will be discussed later, the change in wavelength from red to green light peak emission does create a small proportional shift in the position of the FFT point.
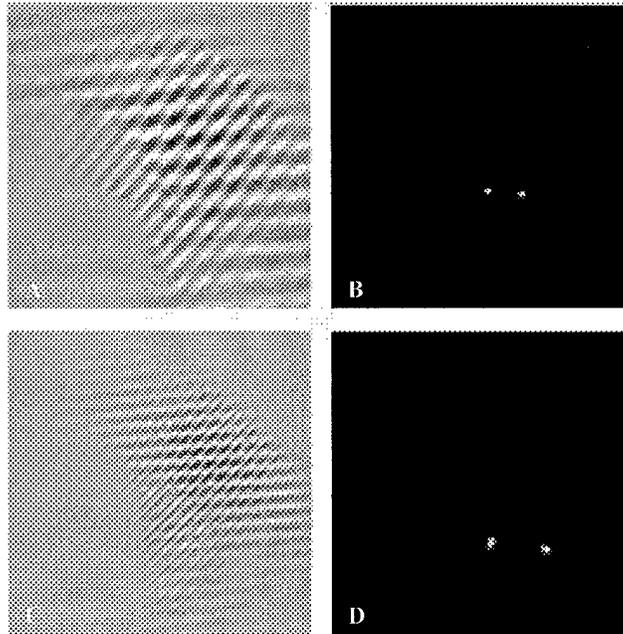
Figure 5.3: The effects of an increase in shear angle. For this comparison, the synthetic binary consists of identical red LEDs with a separation of 1.0 cm, and an angular separation of 237.1 arc-seconds. There is no way to measure the shear angle of the RSI, but the shear angle for images A and B is ~ 5 degrees, and for images C and D the shear angle is ~15 degrees. Images A and C are cumulative fringe patterns and images B and D are their respective FFTs. Note that as shear angle increases the fringe pattern increases in frequency, and the FFT points of the LEDs shift radially away from the center of the FFT.

1.2. Results and Analysis for Varied Shear Angle

For the first experiment the shear angle of the RSI was held constant at ~5 degrees. Unfortunately there is currently no exact way to measure the shear angle of the RSI, so estimation is necessary. Five degrees is considered a low level of shear. For the second experiment, the shear angle was increased to ~15 degrees. Using the synthetic binary of identical red LEDs, the spacing was allowed to vary from 0.7 cm to 1.6 cm as in the first experiment. At each of these separations, Imagekitchen was used to generate a cumulative fringe pattern and perform an FFT. Theory predicts that as the shear angle

increases the fringe patterns of the LEDs will have a higher frequency. The points on the FFT plot will move radially outward from the center of the plot corresponding to the increase in frequency.

This behavior is exhibited in Figure 5.3. In the figure, images A and C are the fringe patterns for the synthetic binary star with a separation of 1.0 cm. The only difference between the two fringe patterns is the increase to the shear angle. As expected, the fringe pattern for the higher shear angle, image C, has a higher frequency than for the lower shear angle, image A. This increase in frequency moves the FFT plot points outward from the center of the image as seen in images B and D. The effect of an increase in shear angle is essentially that of zooming in on the synthetic binary star. Although the spacing of the LEDs has not changed, the change in the frequency of the fringes has blown up the higher shear angle image with respect to the lower shear angle image.

As the shear angle increases, it is expected that the relative spacing between the two synthetic binary points on the FFT shift proportionately. The relative scaling of the points is shown in Figure 5.4. For the low shear angle case, when the spacing between the LEDs changes from 0.7 cm to 1.6 cm the distance between the FFT points almost exactly doubles. With an increase in shear angle, this proportionality should still exist, and it does. The increase in shear angle does not destroy the relative positions of the two points. Given that the two LEDs have the same wavelength, spectral shifts can be ignored and the FFT carries the same spatial information regardless of shear angle changes.
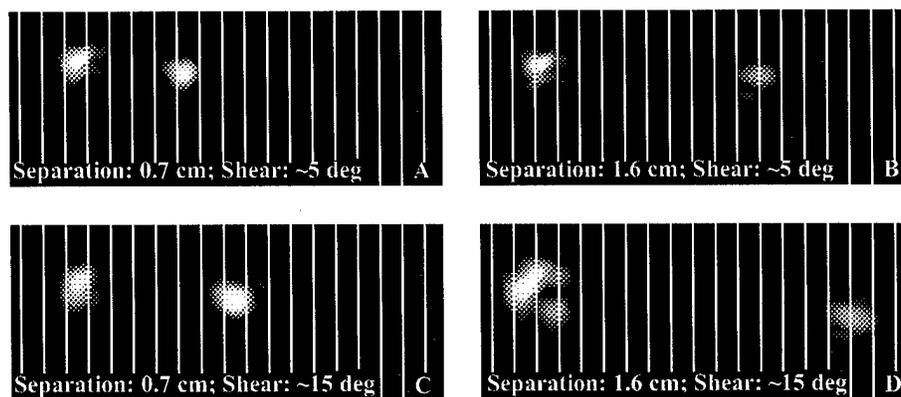
Figure 5.4: As shown in Figure 5.3, as shear angle increases, FFT points move radially away from the center of the FFT plot, thus blowing up the image. Images A and B are taken at a shear angle of ~5 degrees, and images C and D are taken at a shear angle of ~15 degrees. All images are of two identical red LEDs, but in A and C the separation is 0.7 cm, and in B and D the separation is 1.6 cm. The grid lines demonstrate that as the shear angle increases the points move proportionally. In image A the points are 5 lines apart. Moving the LEDs to 1.6 cm apart shifts the FFT points apart by another 5 grid lines. Although the points are relatively farther apart in C and D, the same shift occurs. In image C the points are 8 lines apart. Image D has separation 1.6 cm, and the points are 16 lines apart. Therefore, regardless of shear angle, doubling the separation of the LEDs has the effect of doubling the distance between FFT points (for LEDs with the same wavelength).

2. Two LEDs of Different Wavelength

2.1. Results for a Wavelength Shift

As mentioned previously, when using two identical red LEDs the spectral information contained in the FFT can be ignored, and the relative positions of the LEDs in the synthetic binary are preserved. When one of the red LEDs is replaced by a green LED, this condition is relaxed, and the FFT plot carries both spectral and spatial information. To demonstrate the differences resulting from a shift in wavelength the top red LED was removed from the breadboard, and replaced by a green LED of the type described in Chapter 4. By comparing these fringe patterns and FFT plots to the results for the identical red LEDs, the effects of a change in wavelength can be seen. Figure 5.5 compares the two results. For both of the images, the spacing between the LEDs was held at 1.0 cm. The top LED (the right point on the FFT plot) changed from red in
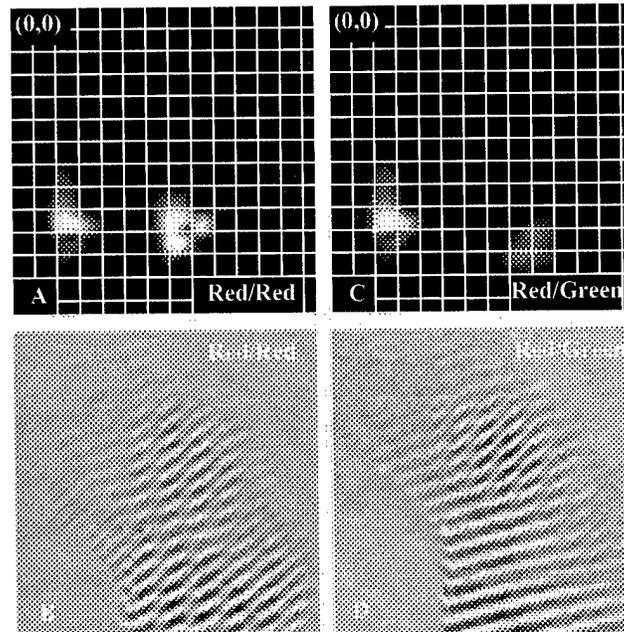
Figure 5.5: The effects of a change in wavelength. Images A and B are of two identical red LEDs placed 1.0 cm apart. Images C and D are of a red LED (left point) and a green LED (right point) at 1.0 cm apart. The only difference between the images is the replacement of the red LED with the green LED in the exact same position on the breadboard. The effects of the wavelength change on the FFT can be seen in images A and C. The green LED's FFT point is down one grid line and moved to the right one grid line of where the red LED is in image A. The zero point for the FFT plot is in the upper left hand corner of images A and C. The radial shift of the FFT points is measured relative to the zero point. This exhibits the radial distance increase expected with a shortening of the wavelength, and predicted in the theory. Notice the two fringe patterns are strong in image B, and in image D the green fringe pattern is much weaker than the accompanying red fringe pattern. This accounts for the change in intensity on the FFT plot.

images A and B to green in images C and D. The resulting shift in the FFT point can be seen by counting the spacing between the two points on the grid. The change in peak wavelength is 75 nm from the red peak at 658 nm to the green peak at 583 nm. As predicted, the shorter wavelength of the green LED shifts the corresponding FFT point radially outward from the center of the FFT plot.

2.2. Analysis for a Wavelength Shift

Theory predicts that the shift of wavelength from red to green will be the same as the shift in distance of the FFT points from the DC spot. Therefore, the ratio between the peak wavelengths of the two LEDs should be the same as the ratio of the radial distances of the red and green LEDs on the FFT plot. First, the ratio of the wavelengths between

the red and green LEDs is $\dfrac{658nm}{583nm}=1.129$. Then, measuring the position of the FFT

points for the red and green LEDs on the zero-padded FFT plot, the distance to the DC

spot can be found. For the red LED, the FFT point is 0.792 inches in the x direction, and

−1.069 inches in the y direction from the center of the FFT plot. This gives a radial

distance of $\sqrt{(0.792in)^2+(-1.069)^2}=1.330in$ for the red LED. For the green LED, the

FFT point is 0.944 inches in the x direction, and −1.167 inches in the y direction from the

center of the plot. This gives a radial distance of $\sqrt{(0.944in)^2+(-1.167)^2}=1.501in$ for

the green LED. The ratio of these distances is $\dfrac{1.501in}{1.330in}=1.129$, a ratio identical to that

for the wavelength peaks. This shows that the radial shift of the FFT point is consistent

with the change in wavelength between the red and green LEDs. The results of a change

in wavelength in the synthetic binary star are consistent with what theory predicts, and

the RSI/telescope combination can handle sources with multiple wavelengths properly.

These results exhibit the degeneracy between spatial and spectral information

described by Gallicchio [4]. When imaging a synthetic binary made of two identical red

LEDs the spatial relationship between the LEDs is preserved in the FFT plot. Since both

of the LEDs have an identical peak wavelength, their radial shift away from the DC spot

on the FFT plot is the same. Therefore the shift due to wavelength can be ignored, and

the plot essentially only contains spatial information. However, when the wavelengths of

the two LEDs in the synthetic binary star are different, then the spectral information

cannot be ignored. The two LEDs will have a different radial position shift due to

wavelength, and the spatial relationship between the points is no longer preserved. As

described in the literature [4], the spatial and spectral information can be separated by

rotating the RSI with respect to the source. Then, since the spectral information of the source has not changed, but the spatial relationship of the source relative to the RSI has changed, the degeneracy can be broken and both a spectral and a spatial plot are obtained simultaneously. Since the RSI/telescope combination will eventually be used in astronomy, the natural progression of the stars across the sky will provide the necessary rotation of the RSI and break the degeneracy.

It is important to note that when the red LED was exchanged with the green LED, the value of "cwave" in the imaging code *telescopealtend2* was not changed. This demonstrates the insensitivity of the wavelength filtering to small changes in the wavelength of the source. As mentioned in Chapter 3, the filtering is successful at removing features from the fringe images that do not change over the course of the "numster" images. However, the filtering does not remove fringe patterns that have a slightly different wavelength from the value in "cwave."

The intensity difference between the FFT points of the red and green LEDs is explained by the accompanying fringe patterns in Figure 5.5. Image B shows the fringe pattern for the two red LEDs. The fringe pattern shows the crisscrossed fringes expected for two sources, and the pattern extends over the majority of the doughnut from the telescope. Image D shows the pattern for the red and the green LED. Unlike image B, the fringe pattern for the red LED extends over the majority of the doughnut pattern, but the fringe pattern for the green LED is limited to a small area in the upper right of the doughnut. Comparatively, the fringe pattern for the green LED is much weaker than that for the red LED, and this implies that the red LED was brighter than the green LED in the synthetic binary. The difference in intensity can be seen in the FFT plots of images A

and C. Image A of the two red LEDs shows two point sources of similar intensity, but image C shows that the green LED was not as bright as the red LED. This demonstrates the RSI/telescope combination's ability to handle sources of differing intensity in the same image. The next step was to test the RSI/telescope combination's ability to handle atmospheric distortion.

3. Distortions due to Atmospheric Turbulence

3.1. Results for Variable Atmospheric Distortion

To generate atmospheric distortions in the lab a hot plate was placed slightly below and in front of a synthetic binary star made out of identical red LEDs at a separation of 0.7 cm as can be seen in Figure 4.3. In the experiment the temperature of the hot plate varied between 150 C and 300 C. This created different levels of atmospheric distortion in front of the synthetic binary star. When the hot plate was at 150 C there were no heat distortions visible to the naked eye above the hot plate, but on the CCD screen the fringe patterns of the two LEDs were noticeably wavering. It is difficult to quantify the level of atmospheric distortion, but as the temperature increased the movement of the fringe patterns on the CCD screen grew more significant. At a temperature of 300 C the heat waves in front of the synthetic binary star were easily visible, and the fringe pattern on the CCD screen was varying on the order of a wavelength.

The RSI/telescope combination took images of the source at each of the four temperature levels. The FFTs of these images can be seen in Figure 5.6. Given that there were significantly different levels of atmospheric distortion between 150 C and 300 C it

is surprising to note that the FFT images are nearly identical across the temperature changes. This implies that the differing levels of atmospheric distortion had no noticeable effect on the cumulative fringe pattern or the FFT plot generated by the Imagekitchen software.
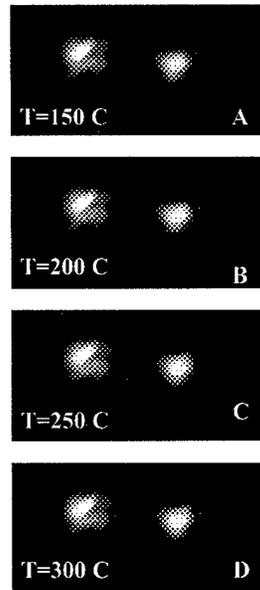
Figure 5.6: Although all of these images appear identical, they are taken with different levels of atmospheric distortion. The synthetic binary was made out of two identical red LEDs separated by 0.7 cm. The hot plate generating the distortion was placed slightly below the level of the synthetic binary as seen in Figure 4.3. At 150 C there is negligible movement in the fringe patterns on the CCD screen, but as temperature increases towards 300 C there is significant fringe motion and distortion. For this reason it is surprising that the cumulative fringe patterns and the FFT plots are almost indistinguishable. It is probable that the low spatial frequency of the source makes it difficult to detect the effects of atmospheric distortion.

3.2. Analysis for Variable Atmospheric Distortion

As discussed at the beginning of Chapter 1, the atmosphere of the earth is constantly changing and distorting starlight as it travels towards earth. This is easily confirmed by looking at a star in the night sky. The twinkling effect is due to the random deflection of star photons as they travel through the earth's atmosphere. Any given star is far enough away from the earth to be considered as a point source. However, any image taken of a star using a ground-based telescope without atmospheric distortion correction

cannot image a star as a point source. Consider a traditional telescope with a CCD camera attached to it that is imaging a star. If there were no atmospheric distortion then every photon from the star that was captured by the telescope would be recorded on the CCD at the same pixel. Looking at the captured CCD image, the star would appear as a single point (1 pixel) on the screen. Now let atmospheric distortion increase. As the distortions increase, each individual photon is deflected and is recorded by the CCD at a slightly different point. This leads to a distribution of photon counts, and the star no longer appears as a single point on the CCD screen. Thus, as atmospheric distortion increases, there is increased blurring of the star image on the CCD screen.

The explanation for the reduced blurring in the RSI/telescope combination's images due to atmospheric distortion is two-fold. First, the source that was imaged during the experiment had low spatial frequency and was not near the resolution limit for the RSI/telescope combination. It is probable that nearer to the resolution limit of the telescope there will be a decrease in image clarity as atmospheric distortion increases. In the future this experiment will be performed again using a source with high spatial frequency.

The second contributing factor towards the reduced distortion due to atmospheric turbulence comes from the way the RSI generates images. As mentioned in Chapter 2, if the RSI is imaging a source which emits a wave of type

$$E(t) = A(t)\exp\{i[\omega_0 t + \phi(t)]\}$$

then dithering one arm with respect to the other changes the relative phase, $\phi(t)$, between the two waves in a predicable way. Although it was not done in this experiment, the predictable change in the phase term can be used to calculate the spectrum of the source.

However, when there is atmospheric distortion the index of the air between the source and the telescope changes with time, and this alters the phase term, $\phi(t)$, of the wave unpredictably. Then, when the RSI dithers one arm, the phase changes no longer directly correspond to the dithering, and the spectral analysis fails. This spectral blurring of the source was not seen in the experiment because only a single wavelength produced the fringes on the CCD screen. The experiment only calculated the spatial position of the source from the cumulative fringe image. The spatial information is recovered from the orientation and frequency of the fringe pattern. Atmospheric distortion does not significantly effect the orientation of the fringes on the CCD screen, and it has no effect on the frequency of the fringes.

To detect blurring due to the small changes in fringe orientation the spatial frequency of the source needs to be high. In this experiment the spatial frequency was low, and neither of the determining factors for the placement of the source points on the FFT plot were changed by the atmospheric distortion. For these reasons there was no blurring of the FFT images due to the high levels of atmospheric distortion between the source and the telescope.

4. RSI/Telescope Resolution

The synthetic binary star used in the experiments had a relatively high angular size relative to the resolution limit of a ground-based telescope. As mentioned in Chapter 1, the resolution limit of a ground-based telescope without atmospheric distortion correction is ~1 arc-second, which is the diffraction limit for a 10 cm telescope. The angular size of the synthetic binary star ranged from 165.7 arc-seconds to 379.4 arc-
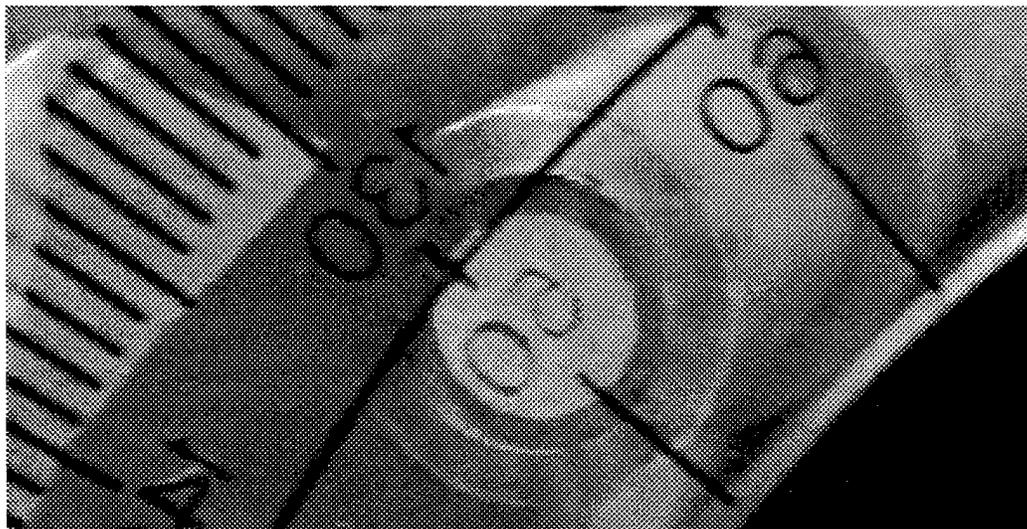
Figure 5.7: The fiber light with a clear protractor in front. The RSI/telescope combination was used to image this source and the FFT plot recovered the number on the protractor. The fiber is 1 cm in diameter, and the number lines have a thickness of approximately 0.6 mm.

seconds. The LEDs were 0.5 cm in diameter, and this put a lower limit on the separation between the LEDs in the synthetic binary. Previous experiments performed on the RSI/telescope using the fiber light provide a better measure of the RSI/telescope's angular resolution. For these experiments, the fiber light was used as the source with a filter in front of the CCD to make the light quasi-monochromatic. A clear protractor was placed in front of the source as seen in Figure 5.7. The RSI/telescope combination was used to image the number on the protractor. The results can be seen in Figure 5.8. The division line has a thickness of 0.6 mm, and the distance to the telescope is 8.7 m, so the angular size of the feature is 14.46 arc-seconds. This is still an order of magnitude above the ground-based resolution limit, but it demonstrates the RSI can image features with a small angular size. Future experiments will use the RSI/telescope combination to image sources with angular size of less than 1 arc-second.
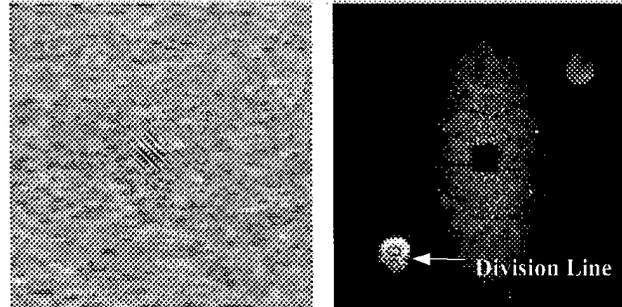
Figure 5.8: Fringe image and FFT plot for the fiber light with a protractor in front. The fiber light is 1.0 cm in diameter. The number 80 on the protractor is in front of the fiber light. The division line below the 80 is 0.6 mm across. The source is at 8.7 meters away from the telescope. This translates into an angular size of 14.46 arc-seconds for the feature on the protractor.

5. Photon Counting

Much of observational astronomy deals with the imaging of dim objects. This places an emphasis on collecting as many photons from a source as possible, and minimizing photon loss. One of the disadvantages of the RSI/telescope imaging system is that there is significant photon loss. This loss stems from many factors. First, every time light is reflected off of a mirror, there is a 5% loss of photons. The imaging system used in this experiment contained 5 mirrors. Next, the telescope aperture is partially blocked by the secondary mirror. Approximately 4% of photons are lost due to this blockage. On the way to the RSI, photons pass through the numerical aperture (NA) matching optics that consists of two glass lenses. There is a photon reflection associated with each glass/air and air/glass interface that creates a 4% loss of photons. There are 10 glass/air and air/glass transitions counting the lenses, the beam splitter, and the right angle mirrors that are glass on the hypotenuse. Then, just by its construction, the RSI reflects 50% of the photons that enter the instrument. When light entering the telescope is not collimated there is leakage around the secondary mirror. This means that some of the light collected by the 10" mirror misses the secondary mirror and exits the front of the telescope instead of the side. This light is not used to generate the fringe image, and for

the source divergence in this experiment ~33 % of the light collected missed the secondary mirror. Finally, to enforce the quasi-monochromatic assumption used in these experiments (when dealing with white light sources) there was a filter with a bandwidth of 12 nm placed in front of the CCD camera that blocked 97% of the visible light spectrum. Not only does the filter block 97% of the visible light, it blocks an additional 50% of photons in the transmission bandwidth. All of these effects together create a 99.76% loss of visible light photons, and only 1 out of every 409 photons is used to generate the fringe pattern on the CCD. This amount of photon loss is enormous compared to the majority of telescope imaging systems, and will limit the ability of the RSI/telescope combination to image dim sources.

6. Conclusion

The experiments and results described above show that the RSI/telescope combination can perform all of the basic imaging tasks required of it in agreement with the theory. The system can image synthetic binary sources with varying degrees of separation. Changes to the shear angle of the RSI produce the expected increase in fringe frequency, and the resulting FFT plots scale to FFT plots taken at lower shear angles. A shift in the wavelength of the source generates a movement away or towards the DC spot of the FFT exactly proportional to the wavelength change. This system can also image multiple point sources with differing intensity simultaneously. Experiment confirmed that the RSI/telescope combination can image sources with angular size one order of magnitude larger than the ground-based resolution limit. The proof of concept phase of this project has demonstrated the RSI suitable for to be adapted for astronomical imaging

purposes. Future experiments will probe the resolution limit of the instrument and measure the sensitivity of the RSI/telescope combination to atmospheric distortion when imaging a source with high spatial frequency. Finally, the astronomical RSI instrument, complete with matching optics, will be coupled to the Three College Observatory 32" telescope and used to image previously unresolvable binary star systems.

7. Acknowledgments

Appendix A

The following is the <u>Mathematica</u> code, titled *abcd numerical aperture*, developed to calculate lens placement distances to match the numerical aperture (NA) of the telescope to the NA of the RSI. The code uses Geometrical Optics and ray tracing to determine the lens placements as described in Chapter 2. The <u>Mathematica</u> input is in **bold** type, and the <u>Mathematica</u> output is in regular type. Different fields of input are separated by blank lines.

```
(* the telescope mirror has a focal length of 45 in, and the tube ends
at 42 in from the plane of the mirror, so measure the effective focal
points from the end of the tube and add 42 in *)

Clear[f1,f2,f3,d1,d2,d3,d4,xf,gf,x0,g0]

trans1 = {{1,d1},{0, 1}};
trans2 = {{1,d2},{0, 1}};
trans3 = {{1,d3},{0, 1}};
trans4 = {{1,d4},{0, 1}};

mirror = {{1, 0},{-1/f1,1}};
lens1 = {{1, 0},{-1/f2,1}};
lens2 = {{1, 0},{-1/f3,1}};

abcd = trans4 . lens2 . trans3 . lens1 . trans2 . mirror . trans1;

ini = {x0, g0};

(* the rhs of the equation *) fin = abcd . ini;

(* x final *) xf = fin [[1]];

(* gamma final *) gf = fin[[2]];

f1 = 48*2.54;

d1 = 45 * 12*2.54;

(* total distance restriction *) dis = d2 + d3 + d4;

x0 = 5*2.54;
g0 = 0;

f2 = 9;
f3 = 15;

(* need to find the numerical aperture for a certain shear angle*)
lambda  = 632.8   (* nm *);
delta   = 9040   (* nm *);
theta   = 15   (* degrees *);
numap   = (-lambda/(delta * Sin[((2 * Pi)/360)* theta]));

f2 = 9;
```

```
f3 = 15;
Clear[d2,d3,d4]
Solve[{ gf == 0, xf == .2*2.54, dis == 80*2.54},{d2,d3,d4}]
{{d4→17.6718,d2→133.846,d3→51.6821}}

(* now check to make sure the size of the beam does not go outside
tolerances at any point along the path *)
(* enter this if you want to clear the variables and see the symbolic
versions of the sizes *)
Clear[f1,f2,f3,d1,d2,d3,d4,xf,gf,x0,g0]


d4 = 17.6718333858267744
d2 = 133.84608
d3 = 51.6820866141732349
17.671833385826774
133.84608
51.682086614173235

(* to find size going into first lens after mirror *)
step1 = trans2 . mirror . trans1 . ini
{-1.2423,-0.104167}

step1xf = step1[[1]]
-1.2423

step1gammaf = step1[[2]]
-0.104167

(* to find size going into second lens after mirror *)
step2 = trans3 . lens1 . trans2 . mirror . trans1 . ini
{0.508,0.0338667}

step2xf = step2[[1]]
0.508

step2gammaf = step2[[2]]
0.0338667

(* to find size going into the rsi, should hold with the above
equations *)
step3 = trans4 . lens2 . trans3 . lens1 . trans2 . mirror . trans1 .
ini
{0.508,0.}

step3xf = step3[[1]]
0.508

step3gammaf = step3[[2]]
0.
```

Appendix B

Mathematica was used for the example in Chapter 3. The code below calculates the focal point of the 10" telescope mirror when the source is a point placed 8 meters from the telescope and 5 cm off of the optical axis. The focal point is found by tracing two rays from the source through the mirror (which is treated as a lens) and calculating their intersection point on the far side of the mirror. The Mathematica input is in **bold** type, and the Mathematica output is in regular type. Different fields of input are separated by blank lines.

```
(* This calculation follows two rays through the optical system and
finds the distance at which the mirror focuses the beam. *)

(* These are the geometrical optics transformation matrices for two
distances and the telescope mirror. *)
trans1= {{1, d1},{0,1}};
mirror= {{1,0},{-1/f,1}};
trans2= {{1, d2}, {0,1}};

(* These are the variable values assuming the mirror is 5 in= 12.7 cm
in radius.  The value for d2 is left unspecified and solved for
later.*)
x1=5 ;
g1= (12.7 - 5)/800;
x2=5;
g2=(-12.7-5)/800;
d1=800;
f=114.3;

(* These are the initial parameters for the two rays traced through the
system. *)
line1={x1,g1};
line2={x2,g2};

(* These give the final position and angle of the two rays. *)
Clear[d2]
fin1=trans2.mirror.trans1.line1;
fin2=trans2.mirror.trans1.line2;

xf1=fin1[[1]];   (* The final position for ray 1 *)

xf2=fin2[[1]];   (* The final position for ray 2 *)

(* Solving for the distance to focus of the source *)
Solve[{xf1 == xf2},{d2}]
{{d2→133.353}}

(* Calculating the distance of the focus off the optical axis *)
d2=133.353;
xf1
xf2
-0.833477
-0.8334353
```

Appendix C

The following is the code for the *autocorrelate* function in <u>Imagekitchen</u>. It is written in the scripting language "Lua," which is similar to C++. This script calculates the wavelength of fringes generated by the RSI in units of voltage applied to the piezo-stage. The input is an operator-defined point on the CCD screen where there is good fringe contrast. The *autocorrelate* function steps through 64 optical path length differences on the piezo-stage and measures the pixel value at each step. If there is fringe variation at the pixel then the resulting plot of pixel intensity versus path length will be sinusoidal. The output is a wavelength, and is used in the imaging code *telescopealtend2* in Appendix D. The *autocorrelate* script was written by Dan Marks.

```
$debug
-- Take autocorrelation of point

cls()
pointx=185
pointy=105
maxwave=100
np=64
centerdist=25000
startdith=centerdist-(maxwave/2)*(np/2)
enddith=centerdist+(maxwave/2)*(np/2)
stepdith = (enddith-startdith)/(np-0.01)

datastor=zeros(1,np)

-- initialize camera
if dev == nil then
  dev = FindDevice("MSVIDEO: Brooktree Bt848 Capture Driver")
  vfwlock = GetDeviceLockId(dev)
  VFWLock(vfwlock)
  ccd_rect = VFWGetCCDRect(vfwlock)
  VFWSetImageConfig(ccd_rect, Pt(0,0), Pt(0,0), vfwlock)
  end

mcaxis=2
if dtdev == nil then
  dtdev = FindDevice("3AxisMirror")
  dtlock = GetDeviceLockId(dtdev)
  MCLock(mcaxis, dtlock)
  end

nf=nil
pf=nil
ps=0

curdith = startdith
while curdith < enddith do
  Alert("Position = "..curdith)
  MCSetAxisValue(curdith,mcaxis,dtlock)
  Wait(2000)
```

```
                    frame = VFWCaptureFrame(vfwlock)

--  Wait(200)
            dp = frame[{pointy,pointx}]
            datastor[{1,ps+1}] = dp
      cnvdata = nil

      if pf == nil then
                    pf = Plot1D(datastor,"Autocorrelation")
      else
                    UpdateDocumentData(pf, datastor)
          end
      cn = nil

      curdith = curdith + stepdith
      ps = ps + 1
      end

if nf ~= nil then
  ReleaseDocument(nf)
        end
ReleaseDocument(pf)
datastor = abs(fft(datastor))
i=0
while i<4 do
  datastor[{1,i+1}] = 0
  datastor[{1,datastor.w-i}] = 0
  i=i+1
  end

datastor=datastor[{1,1,1,datastor.w/2}]
tl = msum(datastor)
xl = msum(lineh(1,datastor.w)*datastor)
xq = msum(absq(lineh(1,datastor.w))*datastor)
Alert("xq = "..xq.." xl = "..xl)
xq = sqrt(xq/tl-(xl*xl)/(tl*tl))
xl = xl / tl
Alert("Center Wavelength: "..((enddith-startdith)/xl).." nm")
Alert("Bandwidth: "..((enddith-startdith)*(1/(xl-xq*0.5)-1/(xl+xq*0.5))).." nm")
Alert("Total signal power: "..tl.." "..xl.." "..xq)
Alert("")
Wait(500)

ReleaseDocument(Plot1D(datastor,"Spectrum"))
```

Appendix D

The following is the Imagekitchen code titled *telescopealtend2*. This is the image collecting code used with the RSI/telescope combination to generate images of a source. It is written in the scripting language "Lua" which is similar to C++. A full discussion of the variables in the code and the operations performed by the code can be found in Chapters 3 and 4. In short, the script captures a series of fringe images from the CCD camera and adds them together with a phase factor to generate a cumulative fringe image. The script takes a Fourier transform of the cumulative fringe image to recover an image of the source. The *telescopealtend2* script was initially authored by Dan Marks, and has been significantly altered by Prasant Potuluri and Bristol Crawford.

```
$debug
-- Image demodulation
cls()
pf=nil
count=0
ps=0
nf=nil
plotman=1
--Wait(40000)
autocorrelate=0
mm=0
nf=0

--filename="G:\\datax\\1-28\\llfile"
-- initialize camera
if dev == nil then dev = FindDevice("MSVIDEO: Brooktree Bt848 Capture Driver")
    --dev = FindDevice("ComputerEyes/PCI Video Capture")
        --dev = FindDevice("Pulnix Camera")
    vfwlock = GetDeviceLockId(dev)
    VFWLock(vfwlock)
    ccd_rect = VFWGetCCDRect(vfwlock)
    VFWSetImageConfig(ccd_rect, Pt(0,0), Pt(0,0), vfwlock)
    end
-- initialize 3axis mirror mcaxis=2 if dtdev == nil then
    dtdev = FindDevice("3AxisMirror")
    dtlock = GetDeviceLockId(dtdev)
    MCLock(mcaxis, dtlock)
    end
-- here we calculate the step size and phase per step npouter=86 datastor=zeros(1,npouter)
npinner=4
numwaves=1
-- one wavelength has a length Length
-- USE THE LINE BELOW FOR BLUE LED
Length=4*250*numwaves
width=512  --dependent on the final frame size
widthx=512
widthy=512
darkly1=zeros(width,width)
darkly2=zeros(width,width)
width1=21  -- area to erase the dc spot
```

```
y1=widthy/2-width1
y2=widthy/2+width1
x1=widthx/2-width1
x2=widthx/2+width1
-- use the line below for red led Length=444*numwaves factor=5
  stepdith=factor*Length/npouter
sp_pi = 3.14159265359
--new for brice's alterations
widthx2=128  --dependent on the final frame size
widthy2=128
width2=11  -- area to erase the dc spot
y21=widthy2/2-width2
y22=widthy2/2+width2
x21=widthx2/2-width2
x22=widthx2/2+width2
--end new code
-- these paremeters are if we want to take an autocorrelation
pointx=171
pointy=111
kark=256
kark2=230


--
sp_dimx = 320              -- x dimension of CCD
sp_dimy = 240              -- y dimension of CCD
sp_begx = 120          -- where to start the sp_finx/y area of the ccd  for white light x80y60
sp_begy = 60           --using x150y1 for the blue leds
sp_finx = 128
sp_finy = 128
sp_dbg=0                   -- is debugging
sp_freq=20


sp_n = 8
sp_cumdata = nil
IM=sqrt(-1)
Wait(100)
count=0
skipskip=1
alpha=1
phase=0
stopnum=npouter
cwave=320  --light wavelength, from autocorrelate
--273 for red interference filter
--320 for red filter
--195 for blue led
--200 for microscope
--281 for red led
--250 for fiber lite
pi_len=cwave/2
  --middith=27450
middith=18000  -- have been using 25000 from autocorrelate function, relative position
--18400 for red led
--23500 FOR WHITE LUGHT AND RED FILTER
--27450 for blue led
-- dithwidth=cwave/2
 dithwidth=(cwave/2)*numwaves
```

```
startdith=middith-dithwidth
enddith=middith+dithwidth
numster=32  --normally 32   --*****
-- start dither loop.
starstar=0
dork=0
sp_frame = VFWCaptureFrame(vfwlock)
while starstar==0 do
  Alert("step num"..count)
dork=dork+1
if dork == 4 then
        dev=nil
        sp_frame=nil
        vfwlock=nil
        ccd_rect=nil
        if dev == nil then
                dev = FindDevice("MSVIDEO: Brooktree Bt848 Capture Driver")
        --dev = FindDevice("ComputerEyes/PCI Video Capture")
                --dev = FindDevice("Pulnix Camera")
        vfwlock = GetDeviceLockId(dev)
        VFWLock(vfwlock)
        ccd_rect = VFWGetCCDRect(vfwlock)
        VFWSetImageConfig(ccd_rect, Pt(0,0), Pt(0,0), vfwlock)
  end
dork=0
end

alpha=alpha+1
if alpha==3 then
  alpha=1
end   --end alpha loop
if alpha==1 then
  delta=pi_len
else
  delta=0
end
if autocorrelate==1 then
  alpha=1
end   --end if autocorr loop

if skipskip==1 then
delta=0
end
curdith=startdith+count*(enddith-startdith)/numster+delta
d1=(curdith-middith)/cwave
phase=2*sp_pi*d1

Alert("Position = "..curdith)
 MCSetAxisValue(curdith,mcaxis,dtlock)
--Wait(1000)
  innercount=0
-- here is where the npinner loop begins.
while innercount<npinner do sp_frame = VFWCaptureFrame(vfwlock)
        --sp_frame= VFWUpdateFrame(vfwlock)
  if sp_frame == nil then
    error("Can not get an image")
```

```
    end  -- end spframe loop

if (autocorrelate==1 and innercount==0) then
        dp = sp_frame[{pointy,pointx}]
        datastor[{1,count+1}] = dp
  cnvdata = nil
  if pf == nil then
                pf = Plot1D(datastor,"Autocorrelation")
  else
                UpdateDocumentData(pf, datastor)
  end  --end pf loop
end
if (innercount==0 and count==0) then

  bere=mmax(sp_frame)
  Alert("value of bere.."..bere)
end

if sp_finx ~= nil then sp_frame = sp_frame[{sp_begy,sp_begy+sp_finy-
1,sp_begx,sp_begx+sp_finx-1}]
  end  --end sp_finx loop
if (count==0 and innercount==0) then cum_frame=sp_frame*expi(phase)
  --  sp_avg=sp_frame
    sp_nf1 = Plot2DIntensity(abs(cum_frame))
else cum_frame=cum_frame+sp_frame*expi(phase)
--  sp_avg=sp_avg+sp_frame
-- UpdateDocumentData(sp_nf1, abs(cum_frame)) end

innercount=innercount+1
end      --end innercount.

-- this is a little subroutine to find where the max value occurs.
--sp_avg=sp_avg*0
-- end sub.
  if (count==0) then
  sp_nf1 = Plot2DIntensity(re(cum_frame),"Final Fringes")
  -- sp_nf6 = Plot2DIntensity(darkly2,"MaxMap") mm=msum(cum_frame)/(128^2)
  -- dg1=abs(fftshift(fft(cum_frame-mm)))
  -- data1=dg1
  -- dg1[{y1,y2,x1,x2}]=dg1[{y1,y2,x1,x2}]*0
  -- sp_nf3 = Plot2DIntensity(dg1,"Final Image") else UpdateDocumentData(sp_nf1,
re(cum_frame))
    -- UpdateDocumentData(sp_nf6, darkly2)
    -- mm=msum(cum_frame)/(128^2)
    -- dg1=abs(fftshift(fft(cum_frame-mm)))
    --data1=dg1
    --dg1[{y1,y2,x1,x2}]=dg1[{y1,y2,x1,x2}]*0
    -- UpdateDocumentData(sp_nf3, dg1)
end
count=count+1
if count>=(numster) then
      starstar=1
  end
end
-- here starts my (brice) spacing of the image
spaced_fr=zeros(512,512)
```

```
--m=1
--n=1
--M=512
--N=512
--spaced_fr = {}
--while n <= N do
--         spaced_fr[n] = {}
--         while m <= M do
--                 spaced_fr[{n,m}] = 0
--                 m=m+1
--         end
--         n=n+1
--         m=1
--end

mm=msum(cum_frame)/(128^2)
cum_frame=cum_frame-mm
mm1=msum(cum_frame)
Alert("mean of cum_frame.."..mm1)
spaced_fr[{1,128,1,128}]=cum_frame[{1,128,1,128}]
--i=1
--j=1
--spaced_fr=cum_frame
--while i <= sp_finy do
--         while j <= sp_finx do
--                 spaced_fr[{2*i,2*j}] = cum_frame[{i,j}] + 5000
--                 --spaced_fr[{4*i,4*j-2}] = 0
--                 --spaced_fr[{4*i,4*j-1}] = 0
--                 --spaced_fr[{4*i,4*j}] = 0
--                 j=j+1
--         end
--         i=i+1
--         j=1
--end
--end of new spaced out frame
--alternate ending
spaceoutput = Plot2DIntensity(re(spaced_fr),"Spaced Out Image")
dg1=abs(fftshift(fft(spaced_fr)))
--dg1=abs(fftshift(fft(spaced_fr)))
dg1[{y1,y2,x1,x2}]=dg1[{y1,y2,x1,x2}]*0 finim=Plot2DIntensity(dg1,"Final Image Large")
dg2=abs(fftshift(fft(cum_frame))) dg2[{y21,y22,x21,x22}]=dg2[{y21,y22,x21,x22}]*0
finim2=Plot2DIntensity(dg2,"Final Image Small") ReleaseDocument(spaceoutput)
ReleaseDocument(finim)
ReleaseDocument(finim2)
--end alternate ending
--summer=0
----sp_nf1 = Plot2DIntensity(re(cum_frame),"Final Fringes")
--mm=msum(cum_frame)/(1)  --dividing factor, divides entire frame,128^2
--dg1=abs(fftshift(fft(cum_frame-mm)))
--data1=dg1
--dg1[{y1,y2,x1,x2}]=dg1[{y1,y2,x1,x2}]*0
--sp_nf3 = Plot2DIntensity(dg1,"Final Image")
```

References

[1] F. Roddier, "Interferometric imaging in optical astronomy," Phys. Rep. **170**, 97-166 (1988)

[2] E. Hecht, *Optics*. Reading, MA: Addison-Wesley, 1998.

[3] G.W. Swenson, Jr., "Radio-astronomy precedent for optical interferometer imaging," J. Opt. Soc. Am. A. **3**, 1311-1319 (1986)

[4] Jason R. Gallicchio, "Spatio-spectral triangulation of visible and infrared point sources using a portable rotational shear interferometer," University of Illinois at Urbana-Champaign, (1999) Masters Thesis

[5] D.L. Marks, R.A. Stack, D.J. Brady, D.C. Munson and R.B. Brady, "Visible Cone-Beam tomography with a lensless interferometric camera," Science **284**, 2164-2216 (1999)

[6] K. Itoh and Y. Ohtsuka, "Interferometric imaging of a thermally luminous two-dimensional object," Opt. Commun. **48**, 75-79 (1983)

[7] R.P. Korechoff, D.J. Diner, E.F. Tubbs and S.L. Gaiser, "Extrasolar planet detection," Astrophysics and Space Science **212**, 369-383, (1994)

[8] K. Itoh and Y. Ohtsuka, "Fourier-transform spectral imaging: retrieval of source information from the three-dimensional spatial coherence," J. Opt. Soc. Am. A. **3**, 94-100 (1986)

[9] M. Murty, "Interference between wavefronts rotated or reversed with respect to each other and its relation to spatial coherence," J. Opt. Soc. Am. **54**, 1187-1190 (1964)

[10] F. Roddier and C. Roddier, "An image reconstruction of Alpha Orionis," Astrophys. J. **295**, L21-L23 (1985)

[11] P. Potuluri, M.R. Fetterman and D.J. Brady, "High depth of field microscopic imaging using an interferometric camera," Optics Express **8**, 624-630 (2001)

[12] K. Itoh, T. Inoue, T. Yoshida and Y. Ichioka, "Interferometric supermultispectal imaging," Appl. Opt. **29**, 1625-1630 (1990)

[13] W.T. Rhodes and J.W. Goodman, "Interferometric technique for recording and restoring images degraded by unknown aberrations," J. Opt. Soc. Am. **63**, 647-657 (1973)

[14] R. Dou, M.A. Vorontsov, V.P. Sivokon and M.K. Giles, "Iterative technique for high-resolution phase distortion compensation in adaptive interferometers," Opt. Eng. **36**, 3327-3335 (1997)

[15] M.S. Scholl and G. Paez, "Cancellation of star light generated by a nearby star-planet system upon detection with a rotationally-shearing interferometer," Infrared Physics & Technology **40**, 357-365 (1999)

[16] R. Guenther, *Modern Optics*. New York, NY: John Wiley & Sons, 1990.